

## Linking Sky-plane Observations of Moving Objects

J. L. TONRY<sup>1</sup>

<sup>1</sup>*Institute for Astronomy, University of Hawaii, 2680 Woodlawn Drive, Honolulu, HI 96822*

(Received Aug 13, 2023; Revised Sep 18, 2023)

Submitted to PASP

### ABSTRACT

The Asteroid Terrestrial-impact Last Alert System (ATLAS) observes the visible sky every night in search of dangerous asteroids. With four (soon five) sites ATLAS is facing new challenges for scheduling observations and linking detections to identify moving asteroids. Flexibility in coping with diverse observation sites and times of detections that can be linked is critical, as is optimization of observing time for coverage versus depth.

We present new algorithms to fit orbits rapidly to sky-plane observations, and to test and link sets of detections to find the ones which belong to moving objects. The PUMA algorithm for fitting orbits to angular positions on the sky executes in about a millisecond, orders of magnitude faster than the methods currently in use by the community, without sacrifice in accuracy. The PUMA software should be generally useful to anyone who needs to test many sets of detections for consistency with a real orbit.

The PUMALINK algorithm to find linkages among sets of detections has similarities to other approaches, notably HeliLinC, but it functions well at asteroid ranges of a small fraction of an AU. PUMALINK is fast enough to test 10 million possible tracklets against one another in a half hour of computer time. Candidate linkages are checked by the PUMA library to test that the detections correspond to a real orbit, even at close range, and the false alarm rate is manageable. Sky surveys that produce large numbers of detections from large numbers of exposures may find the PUMALINK software helpful.

We present the results of tests of PUMALINK on three datasets which illustrate PUMALINK's effectiveness and economy: 2 weeks of all ATLAS detections over the sky, 2 weeks of special ATLAS opposition observations with long exposure time, and 2 weeks of simulated LSST asteroid observations. Detection probabilities of linkages must be traded against false alarm rate, but a representative choice for PUMALINK might be 90% detection probability for real objects while keeping the false alarm rate below 10%. Although optimization of the tradeoffs between detection probability, execution time, and false alarm rate is application specific and beyond the scope of this paper, we provide guidance on methods to distinguish false alarms from correct linkages of real objects.

*Keywords:* astrometry — celestial mechanics — minor planets, asteroids: general

### 1. INTRODUCTION

The Asteroid Terrestrial-impact Last Alert System (ATLAS) has been funded by NASA since 2013 to warn of imminent, destructive asteroid strikes on the Earth. Tonry et al. (2018) described the ATLAS system when it comprised two telescopes on two Hawaiian islands. Since that time two new sites have been commissioned at Sutherland Observatory in South Africa and at El Sauce in Chile, and a fifth ATLAS unit is currently being brought online on Tenerife island at the Teide Observatory (Licandro et al. 2023).

Asteroids smaller than  $\sim 30$  m will mostly explode harmlessly in the atmosphere; larger impactors will generally cause significant damage if they land near a populated area (NRC 2010). The civil defense timescale required to act prior to a predicted impact is at least several days. These two facts determine what the ATLAS etendue (product of sensitivity and area coverage rate) must be. The ATLAS sensitivity is chosen so that it can spot an approaching 30 m asteroid about 3 days before impact<sup>1</sup>, and ATLAS now surveys the visible sky four times every night (weather permitting). These correspond to a best conditions limiting magnitude of  $m_{lim} \sim 19.5$  per exposure and about  $105,000 \text{ deg}^2/\text{day}$  ( $130,000 \text{ deg}^2/\text{day}$  when ATLAS-5 is fully operational).

Coordinating observations and linking detections from different sites around the planet is challenging but offers unprecedented opportunities. ATLAS is in the process of updating its scheduler to take advantage of this, and this paper introduces a new, inter-day linking algorithm to support this development.

There are a number of other ongoing sky surveys, notably PanSTARRS-1 and PanSTARRS-2 (Chambers et al. 2016) ( $m_{lim} \sim 22.5$  and  $8,000 \text{ deg}^2/\text{day}$ ), the Catalina Sky Survey ( $m_{lim} \sim 21.3$  and  $3,600 \text{ deg}^2/\text{day}$ ) (Drake et al. 2009), the Zwicky Transient Facility ( $m_{lim} \sim 20.5$  and  $40,000 \text{ deg}^2/\text{day}$ ) (Bellm et al. 2019; Graham et al. 2019), and ASASSN ( $m_{lim} \sim 18$  and  $200,000 \text{ deg}^2/\text{day}$ ) (Kochanek et al. 2017). The LAST survey (Ofek et al. 2023) is just getting started but its wide field mode should produce  $m_{lim} \sim 21$  and  $18,000 \text{ deg}^2/\text{day}$ . In a few years the Rubin Telescope will start its LSST survey ( $m_{lim} \sim 23.5$ , the single exposure 5-sigma point source depth averaged over all six filters weighted by the number of visits per lunation) and  $8,000 \text{ deg}^2/\text{day}$ ) (Ivezić et al. 2019). Finding dangerous asteroids is a significant mission for all of these surveys.

After data collection, surveys calibrate the astrometry and photometry of each image, and then detect as many objects as possible, tabulating their position, brightness, as well as attributes such as size and shape. Difference imaging, i.e. matching and subtracting a static sky image taken some time previously, is an effective technique to support the detection of transient, variable, or moving objects. Implementations include Alard & Lupton (1998), Becker et al. (2015), and Zackay et al. (2016). This is helpful for suppressing detection of static objects, but equally important is the reduction of the influence of bright static objects on the astrometry and photometry of non-static objects. No matter the survey, the majority of detections are very faint and appear at the signal-to-noise ratio (SNR) limit, loosely defined as the point where the probability of detection is distinctly less than unity, and the false alarm rate (random and systematic) becomes significant.

When a survey collects multiple exposures, the probability of detecting an object on one or more exposures is improved, and the probability that false alarms, consistent with a single object, appear on two or more exposures is reduced. Deciding whether detections from multiple exposures belong to a single object is the “linking problem”. The uncertainty in the location of a point-like object is approximately its full width half maximum (FWHM) extent divided by the detection SNR, and for a stationary object the probability of a false linkage between two observations is this solid angle times the angular density of spurious detections. Linking moving objects is more difficult because the solid angle available for linking detections is stretched by the angular velocity of the object times the interval between exposures. If the direction and speed of the object is unknown this solid angle can be substantial.

There is an upper limit to an object’s angular velocity that must be considered. If an object moves fast enough its appearance on an exposure will be detectably trailed (roughly one FWHM per exposure time at the SNR limit). This rate is of order  $\omega \sim 1 \text{ deg/day}$  ( $2.5 \text{ arcsec/min}$ ) for seeing limited surveys such as Pan-STARRS or LSST, or  $\omega \sim 4 \text{ deg/day}$  for a pixel limited survey such as ATLAS. As a linking strategy, objects that are detectably trailed should be sorted into a special subgroup for intercomparison, greatly reducing the false alarm density.

False alarm detections arise from many sources: imperfect subtractions, detector artifacts, cosmic rays, optical ghosts and glints, satellite trails, etc, as well as detections of real objects that happen to be coincident with a different object. For example, a typical detection density in an ATLAS difference image might be  $200 \text{ deg}^{-2}$ , of which only 10% might be real objects. It is useful to apply a classification filter on detections before moving on to linkage: most false detections are visibly false to a human being, so machine learning approaches to classification can be extremely effective (Chyba Rabeendran & Denneau 2021).

The density of false alarms caused by real objects is highly variable. For example Heinze et al. (2018) found the density of suspiciously variable objects to be  $n \sim 20\text{--}1000 \text{ deg}^{-2}$ , depending on galactic latitude, to a limiting magnitude of about 18 away from the galactic plane and 17 near the plane.

<sup>1</sup> observing  $90^\circ$  from the Sun; warning time in other directions varies with the asteroid illumination

The physical density of known main belt asteroids in the ecliptic plane ( $2.5 \text{ AU} < r < 3.0 \text{ AU}$  and  $-0.2 \text{ AU} < z < +0.2 \text{ AU}$ ) found in the `astorb.dat` database<sup>2</sup> can be roughly described as

$$n(<D) \sim 300,000 \text{ AU}^{-3} \left( \frac{D}{1\text{km}} \right)^{-2} \quad (1)$$

( $D$  is the asteroid diameter), which integrates to an angular density of about  $150 \text{ deg}^{-2}$  for 1 km asteroids at a limiting magnitude of 21.5–23.5 (depending on viewing phase angle), or  $\sim 4 \text{ deg}^{-2}$  for  $\sim 6 \text{ km}$  asteroids visible to ATLAS at opposition. For evaluating moving object densities at higher ecliptic latitude and angular velocity, the density of asteroids near the Earth from `astorb` is approximately

$$n(<D) \sim 150 \text{ AU}^{-3} \left( \frac{D}{1\text{km}} \right)^{-2} \exp\left(-\frac{|z|}{0.14\text{AU}}\right). \quad (2)$$

(Note that this is the instantaneous density; the count of all near Earth objects (NEO) whose orbits bring them within 0.3 AU of the Earth’s orbit, for example, is about 6 times greater.)

It is more difficult to link moving objects at a finite distance with non-contemporaneous observations because the observations need to constrain an angular velocity as well as a position, and because the object’s unknown velocity allows confusion by false alarms from a larger solid angle.

Any 3 coordinates on the sky supply the 6 constraints necessary to formally solve for a three dimensional (3D) orbit that links them. Orbits through unrelated detections can mostly be rejected because of wildly unphysical velocities for example, or a sub-Earth surface perigee between the three points, but there is no way to assess goodness of fit for an orbit through three points and orbits which differ in radial distance and velocity are highly degenerate.

If a survey covers a solid angle  $\Omega$  in a night with a detection angular density  $n$ , the number of pairs to be considered up to an angular velocity  $\omega$  over an inter-exposure time  $\delta t$  is  $N_{\text{pair}} \sim \Omega \pi (\omega \delta t)^2 n^2$ , which can be considerably greater than 1 million for a typical survey.

Propagating each pair to the time of a third detection and requiring a new detection at the extrapolated location multiplies the numbers by a factor of  $\pi \delta \theta^2 n$ , where  $\delta \theta$  is the typical astrometric uncertainty that grows over the interval from the pair to the third (with allowance for all reasonable orbits). This factor grows quadratically with time and is typically very small for time intervals less than an hour and very large for time intervals greater than a day.

This factor is the crux of strategies to link detections of moving objects. On the one hand, collecting a third point quickly after a pair lowers the false alarm rate, and collecting a fourth lowers the false alarm rate again and permits a statistical evaluation of whether the best-fit orbit is consistent with the observations. Bright or trailed detections may have a low enough angular density that only 3 detections are required.

On the other hand, relaxing the requirement for 4 quickly spaced observations permits more sky to be covered, and requiring 4 detections can be costly for detection probability near the SNR limit. For example, if there are 4 observations on which an object might be detected with a probability of 0.8, the probability that it is in fact detected 4 times is only 0.4. The probability of obtaining at least 4 detections can be increased to 0.8 by taking 5 observations, but at the cost of decreasing the time available to cover more sky by 20%.

The Moving Object Processing System (Denneau et al. 2013), is used very successfully by most asteroid surveys, including Pan-STARRS, the Catalina Sky Survey, and ATLAS. In its original design, when Pan-STARRS was slated to comprise 4 telescopes on Maunakea, MOPS expected to process pairs of detections from at least three nights from a lunation. (Naively this would consume  $\mathcal{O}(N^3)$  computation time, where  $N$  is the number of pairs, but this was deemed to be computationally tractable.)

When Pan-STARRS became operational with only 1 telescope, the combination of losses from fill factor, weather, and schedule made this “three tracklet” approach unproductive, and Pan-STARRS switched to an “extrapolated arc” approach, concentrating four exposures into only an hour. The ATLAS version of MOPS is also mindful of the detection density and can officially declare a linkage for only 3 detections if they are bright or trailed enough. However, the majority of detections are faint and not detectably trailed, so a full set of 4 detections is required.

A nice strategy for linking detections across a substantial time interval arises when they are grouped as pairs of “tracklets” (a tracklet is two or more linked detections), and explicitly using the angular velocity of the tracklet as

<sup>2</sup> [asteroid.lowell.edu/main/astorb](http://asteroid.lowell.edu/main/astorb)

well as its location on the sky. [Bernstein & Khushalani \(2000\)](#) used this method to extend short arc detections of Kuiper Belt objects (KBO). The [Bernstein & Khushalani \(2000\)](#) approach was designed to guide new observations to recover outer solar system objects with uncertain orbits, and it exploited pairs of detections to provide a location and a velocity. Their motivation was linking very slow moving objects in order to guide future observations with a small field of view.

More recently and generally [Holman et al. \(2018\)](#) describe an algorithm called “HelioLinC” to link pairs of detections over time intervals of many days. HelioLinC goes a step farther than [Bernstein & Khushalani \(2000\)](#) and links tracklets that may be moving rapidly and not on a great circle.

HelioLinC’s approach is to transform the detections on the sky to a 3D location in the solar system, using the Sun as the origin, so that object’s trajectories lie on a great circle (neglecting Earth and Moon gravity), with angular velocity consistent with a Keplerian orbit. HelioLinC must assume a distance and radial velocity to perform this transformation, but the subsequent linking problem becomes very simple because each tracklet can be advanced along its orbit to a reference time, and comparison of all tracklets at the reference time lends itself to sorting and  $N \log N$  execution time.

This comparison can be quick enough that it is possible to explore a number of different assumptions for distance and radial velocity. Because the tracklets can be actually propagated along an orbit, there is no restriction that the observations of different tracklets be particularly close in time — matching two tracklets from anywhere during a lunation is easy. [Holman et al. \(2018\)](#) demonstrated the HelioLinC performance on objects ranging from the outer solar system down to near Earth objects that are fairly close (closer than 1 AU).

Yet another approach by [Moeyens et al. \(2021\)](#) called “THOR” links detections without requiring any organization into tracklets, instead computing proximity relative to a set of presupposed trial orbits. THOR is especially useful for Main Belt asteroids where Jupiter’s gravity may be important because the distance makes the angular variation among a modest number of trial orbits relatively small. It is considerably more difficult and resource consuming for THOR to include enough NEO orbits to link objects that are close to the Earth. This is a disadvantage for the ATLAS mission of finding and linking approaching impactors.

The unique advantage of THOR is the ability to link single detections, but the price is that THOR is resource intensive. The experiment described by [Moeyens et al. \(2021\)](#) linking a lunation of ZTF data consumed 10M core-seconds, whereas the PUMALINK algorithm described here would complete in about 10k core-seconds, 3 orders of magnitude faster. However, without the organization of ZTF observations into pairs separated by no more than a few hours, PUMALINK would not work at all.

Each of these algorithms, MOPS, HelioLinC, and THOR has regimes of utility. In its current incarnation MOPS requires 4 detections over a short period of time, but MOPS is highly efficient and functions well for objects even closer than the Moon. HelioLinC requires only pairs of detections, but the tracklets can come from different observatories and from times separated by days or weeks. THOR does not even require observations organized into tracklets, but is quite resource intensive. Both HelioLinC and THOR make approximations that hamper their effectiveness for asteroids which are close to the Earth and feel the gravity of of Earth and Moon.

Neither MOPS nor HelioLinC is ideal for the ATLAS mission. The false alarm rate for faint pairs or triples inhibits ATLAS from submitting them to the Minor Planet Center (MPC) for eventual linkage with other, dubious pairs or triples, even though the combination may be completely beyond question. ATLAS also needs to recognize and link very nearby asteroids, even closer than 0.04 AU (one week before impact), and HelioLinC does not perform well in that regime. In addition, collection of 4 observations every night to satisfy MOPS is costly. If ATLAS can provide 3 days warning of a 30 m asteroid on a 1 day cadence by using MOPS and 4 detections per night, would it be not be better to quadruple the exposure time but only take two observations every other night? The 2 day cadence can cost 1 day of lost time, but the quadrupled exposure time means that the asteroid will first be detected when it is 6 days distant, and its SNR will be doubled when it is 3 days distant. All that is required for this improvement is a multi-day linkage scheme that is reliable at distances less than 0.04 AU.

For many years ATLAS has used an algorithm called “Position Using Motion with Acceleration” (PUMA) for rapidly testing whether multiple detections follow a consistent trajectory (i.e. orbit fitting). This code evolved from software that was originally developed to fit high precision orbits to artificial satellites, so it does not use orbital propagation approximations such as Keplerian, and it is extremely efficient. PUMA has three notable features: it is very fast (a handful of detections can be tested for a consistent orbital trajectory in a millisecond), it takes full advantage of the observational uncertainties, and it functions well at distances down to the surface of the Earth.

We have recently extended the PUMA approach to the linking problem, calculating when pairs of pairs of detections form a consistent orbit. The second section of this paper describes the PUMA method for fitting an orbit to a set of detections, the third section describes this new PUMALINK approach to linking pairs of detections, and the fourth section details the results of a number of tests.

The PUMA and PUMALINK code may be found on [github](https://github.com/atlas-ifa/puma)<sup>3,4</sup>.

## 2. THE PUMA LIBRARY

The PUMA computation strategy is to determine a range from observer to object for each observation using the Earth-Moon barycenter as the origin. Given the range of the object at each observation, it is quick to determine an orbit that best threads through the (now) 3D observed locations. The displacement of the observer from the E-M barycenter is known at all times, and the non-inertial motion of the E-M barycenter is smooth enough to be described by a polynomial for a substantial fraction of a year.

### 2.1. Definitions

Starting with some definitions, suppose we have observations at different times  $t'_i$  of an object that emitted light at instants  $t_i$ . Let the (known) observer locations in the solar system at times  $t'_i$  be  $\mathbf{O}'_i$ , the (accurately known, unaberrated) sight lines from observer at time  $t'_i$  to object at time  $t_i$  be  $\hat{\mathbf{u}}_i$ , and the (unknown) ranges between the object at time of emission and the observer at time of observation be  $r_i$ . ( $\hat{\mathbf{u}}_i$  and  $r_i$  span events between emission and receipt of light so we omit primes for their symbols.) This is illustrated in Figure 1.

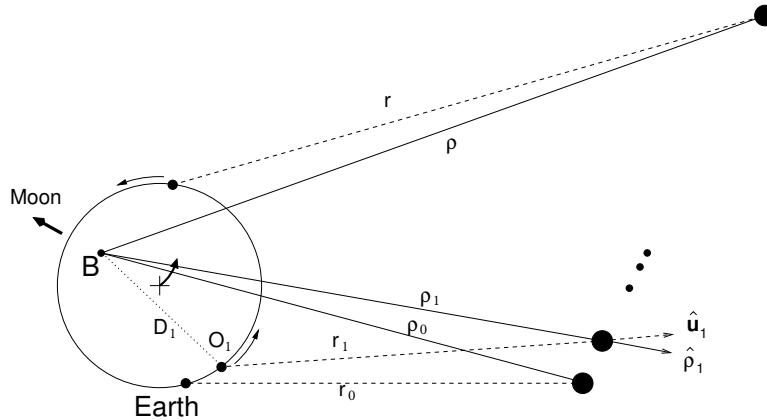


**Figure 1.** The motion of an asteroid with respect to the Earth-Moon barycenter is viewed from an observatory on the rotating surface of the Earth which itself orbits the E-M barycenter. The object is observed at ranges  $r_i$  from the observatory locations  $\mathbf{O}'_i$  in directions  $\hat{\mathbf{u}}_i$  at times  $t'_i$ . The displacement from E-M barycenter to the observatory  $\mathbf{D}'_i$  is accurately known, and the distances and unit vector from barycenter to object are  $\rho_i$  and  $\hat{\rho}_i$ . (For clarity some variable's primes are omitted and the orbit of the non-inertial E-M barycenter around the Sun is not indicated.)

The Earth-Moon barycenter location in the solar system at time  $t'_i$  is denoted as  $\mathbf{B}'_i$ , the displacement between observation and barycenter is  $\mathbf{D}'_i = \mathbf{O}'_i - \mathbf{B}'_i$ , and we describe the distance between E-M barycenter and object as  $\rho_i$ . (We ignore the few milliseconds of light travel time between observer and barycenter, and we use *range* to describe observer-object and *distance* for barycenter-object displacements.) Given a distance  $\rho$  it is straightforward to solve for the observer-object range using the law of cosines:

$$r = [\rho^2 - D_{\perp}^2]^{1/2} - D_{\parallel}, \quad (3)$$

where  $D_{\perp}$  and  $D_{\parallel}$  are the perpendicular and parallel projections of  $\mathbf{D}'$  relative to  $\hat{\mathbf{u}}$ .

<sup>3</sup> <https://zenodo.org/badge/latestdoi/674389255>

<sup>4</sup> <https://github.com/atlas-ifa/puma/tree/main>

The solar system locations of the object are therefore  $\mathbf{x}_i = \mathbf{O}'_i + r_i \hat{\mathbf{u}}_i$ , and the times are related by  $t_i = t'_i - r_i/c$ . The unit vector from E-M barycenter to object is

$$\hat{\boldsymbol{\rho}}_i = \frac{\mathbf{O}'_i + r_i \hat{\mathbf{u}}_i - \mathbf{B}'_i}{|\mathbf{O}'_i + r_i \hat{\mathbf{u}}_i - \mathbf{B}'_i|}. \quad (4)$$

As an example, given three observations of an object moving at constant velocity in the solar system at a distance such that the change in light travel time is small compared to the interval between observations, it is simple to calculate the three ranges. Define the time ratio as  $\lambda = (t_2 - t_0)/(t_1 - t_0)$  and the triple product of the unit vectors as  $T = \hat{\mathbf{u}}_0 \times \hat{\mathbf{u}}_1 \cdot \hat{\mathbf{u}}_2$ . Then

$$\begin{pmatrix} r_0 \\ r_1 \\ r_1 \end{pmatrix} = \frac{1}{\lambda(\lambda - 1)T} \begin{pmatrix} -\lambda \hat{\mathbf{u}}_1 \times \hat{\mathbf{u}}_2 & \rightarrow \\ (\lambda - 1) \hat{\mathbf{u}}_2 \times \hat{\mathbf{u}}_0 & \rightarrow \\ -\lambda(\lambda - 1) \hat{\mathbf{u}}_0 \times \hat{\mathbf{u}}_1 & \rightarrow \end{pmatrix} \begin{pmatrix} (\lambda - 1) \mathbf{O}'_0 - \lambda \mathbf{O}'_1 + \mathbf{O}'_2 \\ \downarrow \end{pmatrix}. \quad (5)$$

The right arrows ( $\rightarrow$ ) and down arrows ( $\downarrow$ ) indicate that the vector components are distributed into a row or column respectively. From this we immediately see that if the unit vectors  $\hat{\mathbf{u}}_0$ ,  $\hat{\mathbf{u}}_1$ , and  $\hat{\mathbf{u}}_2$  are co-planar and  $T = 0$  (i.e. no relative acceleration between observer and object) the three ranges  $r_i$  are indeterminate. A least squares solution for more than three observations has the same property for co-planar  $\hat{\mathbf{u}}_i$ .

If  $T \neq 0$  it is possible to solve this equation, at least formally, but the errors in the  $\hat{\mathbf{u}}_i$  will be magnified by  $1/T$ , so we want  $T$  to be as big as possible, which requires some non-linearity (acceleration) in the relative motion of observer and object. Apart from non-linear motion of the object, observations may happen from different points on (or off) the Earth, the observer-object range has a 24 hour sinusoidal component of amplitude  $\sim 5,500$  km from the Earth's spin, the Earth's orbit around the Earth-Moon barycenter creates a monthly sinusoidal component of order  $\sim 4,700$  km, and the sagitta of the Earth's motion around the Sun over one day is  $\sim 5,700$  km. All of these contribute to non-linear motion of the observer-object separation, but they take time to build up, which makes the linking problem worse.

## 2.2. PUMA

The key to the PUMA strategy is to determine the scalar distance function  $\rho(t)$  from E-M barycenter to object because it allows us to place the angular observations  $\hat{\mathbf{u}}_i$  into 3D space where it is easy to fit an orbit. By design this function  $\rho(t)$  can be very well approximated by a polynomial in time for a fraction of a year. As we shall see, the choice of the Earth-Moon barycenter as the origin instead of the Sun makes the result much less sensitive to the distance and radial velocity of the object. PUMA calculates in J2000 solar system ecliptic coordinates.

The PUMA library proceeds iteratively to find the function  $\rho(t)$ , based on assumed values for  $\rho_0$  and  $\dot{\rho}_0$  at a reference time  $t_0$ . The object's orbit may be very non-linear, particularly when it passes close to the Earth, seen both in angular observations that deviate from a great circle as well as distance  $\rho(t)$  that may so non-linear as to pass through a minimum.

The normal approach of a differential equation integrator is to start from an initial condition and propagate in time by short, polynomial steps that are brought into consistency by calculating the acceleration at a set of test points.

By contrast PUMA is exploiting a set of extremely accurate angular positions at known times (to within slight perturbations from differential light travel time), and it only calculates accelerations at those times along the trajectory. Rather than building a piece-wise set of polynomials that can approximate an arbitrary function, PUMA uses an origin such that a single polynomial in distance suffices.

PUMA starts with a linear polynomial for the distances at the times of observation,  $\rho_i = \rho_0 + \dot{\rho}_0(t_i - t_0)$ , clipped at  $\rho_i > 0.001\rho_0$ . Using these distances and therefore the 3D locations  $\mathbf{x}_i$  of the object in the solar system, the accelerations  $\ddot{\mathbf{x}}_i$  of the object due to the gravity of the Sun, Earth, and Moon are evaluated. (The location  $\mathbf{B}_i$ , velocity  $\dot{\mathbf{B}}_i$ , and acceleration  $\ddot{\mathbf{B}}_i$  of the E-M barycenter are known.)

The second derivative of the displacement vector  $\boldsymbol{\rho}$  from E-M barycenter to object location is just  $\ddot{\boldsymbol{\rho}} = \ddot{\mathbf{x}} - \ddot{\mathbf{B}}$ . The second derivative of the scalar  $\rho(t)$  is then

$$\ddot{\rho} = \frac{d^2}{dt^2}(\boldsymbol{\rho} \cdot \boldsymbol{\rho})^{1/2} = \hat{\boldsymbol{\rho}} \cdot \ddot{\boldsymbol{\rho}} + \rho |\dot{\hat{\boldsymbol{\rho}}}|^2, \quad (6)$$

i.e. the projection of the second derivative of  $\boldsymbol{\rho}$  onto the radial direction compensated by the centrifugal acceleration. In order to determine  $\rho(t)$  we need the physical acceleration of observer and object as well as the angular velocity.

Although the orbit does not project to a perfect great circle as viewed from the E-M barycenter, an approximate great circle fit provides an adequate measure of the angular velocity required by Eq 6 because the progress along the great circle fit is allowed to vary, anchored by the all the observations. If the unit vectors from barycenter to object  $\hat{\rho}_i$  have uncertainties  $\delta\theta_i$  we can find a great circle with pole  $\hat{\mathbf{g}}$  that most closely passes through the points. Form a “great circle merit function”

$$\chi_g^2 = \Sigma(\hat{\mathbf{g}} \cdot \hat{\rho}_i)^2(\delta\theta_i)^{-2} \quad (7)$$

that sums the squared deviations of the points from the equator of this great circle. The least squares solution is

$$0 = \begin{pmatrix} b_{xx} & b_{xy} & b_{xz} \\ b_{yx} & b_{yy} & b_{yz} \\ b_{zx} & b_{zy} & b_{zz} \end{pmatrix} \begin{pmatrix} g_x \\ g_y \\ g_z \end{pmatrix}, \quad (8)$$

where  $b_{jk} = \Sigma\hat{\rho}_j\hat{\rho}_k(\delta\theta_i)^{-2}$ . This is singular because it does not incorporate the constraint that  $|\hat{\mathbf{g}}| = 1$ . Rather than imposing this via Lagrange multiplier or a quadratic ( $|\hat{\mathbf{g}}|^2 - 1$ ) term simply set  $g_k = 1$  for the  $k$  with minimal  $|b_{kk}|$ , solve for the other two components, and renormalize. Because the  $\delta\theta$  are so small this causes negligible error.

Once the great circle pole is known, the azimuthal angle of each observation around the great circle with respect to a reference observation at  $t_0$  can be estimated from the normals  $\hat{\mathbf{n}}_i$  to the planes defined by  $\hat{\mathbf{g}}$  and  $\hat{\rho}_i$ :

$$\hat{\mathbf{n}}_i = \frac{\hat{\mathbf{g}} \times \hat{\rho}_i}{|\hat{\mathbf{g}} \times \hat{\rho}_i|}, \quad \phi_i = \tan^{-1}(\hat{\mathbf{n}}_i \cdot \hat{\mathbf{g}} \times \hat{\mathbf{n}}_0, \hat{\mathbf{n}}_i \cdot \hat{\mathbf{n}}_0). \quad (9)$$

This set of  $\phi_i$  is fitted with a polynomial in  $t_i - t_0$ , and its derivative provides a measure of the instantaneous angular velocity. The PUMA library will use up to a cubic polynomial, given 4 or more observations at diverse times, because this “along track acceleration” can change rapidly when an asteroid ventures near the Earth-Moon system.

If desired, the great circle fit to the unit vector  $\hat{\rho}$  at any given time along the great circle may be calculated from the pole  $\hat{\mathbf{g}}$ , the point on the great circle at the reference time  $\hat{\mathbf{h}}_0 = \hat{\mathbf{n}}_0 \times \hat{\mathbf{g}}$ , and the angle  $\phi(t_i - t_0)$ ,

$$\hat{\rho} = \cos\phi \hat{\mathbf{h}}_0 + \sin\phi (\hat{\mathbf{g}} \times \hat{\mathbf{h}}_0). \quad (10)$$

and this can be compared with  $\hat{\rho}_i$ . The PUMA library makes this available to the user although it is not used otherwise.

This first iteration with a linear  $\rho(t)$  now provides values for  $\ddot{\rho}_i$  and we iterate a second time with a quasi-cubic fit for  $\rho(t)$  that provides new predictions at the time of each observation using a linear change in acceleration between the reference time and each observation,

$$\rho_i - \rho_0 = \dot{\rho}_0(t_i - t_0) + \frac{1}{3}(\ddot{\rho}_0 + \frac{1}{2}\ddot{\rho}_i)(t_i - t_0)^2. \quad (11)$$

(For clarity we do not show the factor of  $(1 + \dot{\rho}_0/c)$  that needs to multiply  $(\rho_i - \rho_0)$  to express the light travel time  $t'_i - t_i$ .)

For most purposes and for distances greater than 0.01 AU Eq. 11 suffices. However, when an object comes very near the Earth it is necessary to add a quadratic term to the distance acceleration of Eq 11. The PUMA library implements this (when there is sufficient time diversity) by fitting a quadratic function to all the gravitational acceleration values, evaluating  $\ddot{\rho}$  as a quadratic function of time, and integrating it twice as in Eq. 11 to obtain each  $\rho_i$  from a quartic polynomial for  $\rho(t)$ . Such a quadratic acceleration correction is iterated twice.

Given this assumption for a distance and radial velocity  $\rho_0, \dot{\rho}_0$ , the function  $\rho(t)$  allows us to do a least-squares solution for the state vector  $(\mathbf{x}_0, \mathbf{v}_0)$  that describes the trajectory that is most consistent with the observations. We expect that the object trajectory in the solar system is

$$\mathbf{x}(t) = \mathbf{x}_0 + \mathbf{v}_0(t - t_0) + \frac{1}{2}\mathbf{a}_0(t - t_0)^2 + \frac{1}{6}\mathbf{a}_1(t - t_0)^3 + \frac{1}{12}\mathbf{a}_2(t - t_0)^4, \quad (12)$$

where the acceleration encountered along the trajectory is

$$\mathbf{a} = \mathbf{a}_0 + \mathbf{a}_1(t - t_0) + \mathbf{a}_2(t - t_0)^2.$$

( $\mathbf{a}_2 = 0$  if there are fewer than 3 time diverse observations.)

Note that the distances  $\rho_i$  and ranges  $r_i$  have already been evaluated for this assumed  $\rho_0, \dot{\rho}_0$ , and the accurately known  $\hat{\rho}_i$  implies that the acceleration coefficients,  $\mathbf{a}_0$ ,  $\mathbf{a}_1$ , and  $\mathbf{a}_2$ , are already accurately known for whatever best fit  $\mathbf{x}_0, \mathbf{v}_0$  will emerge. Since we can treat  $\mathbf{a}_0$ ,  $\mathbf{a}_1$ , and  $\mathbf{a}_2$  as constant, the predicted  $\mathbf{x}(t_i)$  are then linear functions of the state vector as are the predicted observed unit vectors  $(\mathbf{x}(t_i) - \mathbf{O}'_i)/r_i$  so these unit vectors can be compared with the observed unit vectors through an appropriate inverse covariance matrix to form a  $\chi^2$  merit function similar to Eq 7. In the PUMA library it is advantageous to distinguish along-track versus cross-track errors because these differ for streaked detections. Setting the derivatives of  $\chi^2$  with respect to  $(\mathbf{x}_0, \mathbf{v}_0)$  equal to zero provides equations for the best fit  $(\mathbf{x}_0, \mathbf{v}_0)$ , and the minimum value of  $\chi^2$  provides an assessment of whether the assumed  $(\rho_0, \dot{\rho}_0)$  are a reasonable match to the data.

Of course finding the  $(\mathbf{x}_0, \mathbf{v}_0)$  that best threads through the observed angular positions, given that the radial distance and velocity are essentially fixed, is really a 4D angular problem, but it is computationally more efficient to solve the three, linear, Cartesian position–velocity equations, not to mention avoiding the singularity at the poles.

This solution at an assumed  $(\rho_0, \dot{\rho}_0)$  differs slightly from an exact orbital trajectory that could be obtained by classic differential equation integration in two ways: the acceleration along the trajectory is fitted as a first or second order polynomial, and the acceleration is derived using a distance function that is also a polynomial. Even if the iteration to this solution converges, the orbit and object locations at times  $t_i$  are slightly different from actuality. Within the domain of validity for PUMA, the difference is much less than ground-based observational error, however.

Given  $\chi^2(\rho_0, \dot{\rho}_0)$ , a non-linear least squares fit for a best fit  $(\rho_0, \dot{\rho}_0)$  is straightforward, although a few technical details are important. The fitted variables are actually  $\ln(\rho_0)$  and  $(\dot{\rho}_0/\rho_0)$  in order to keep  $\rho_0$  positive and avoid the large covariance between  $\rho_0$  and  $\dot{\rho}_0$ . A grid search for initial conditions and priors on  $\rho_0$  and  $\dot{\rho}_0$  can help prevent the best fit solution from running away to unreasonable values.

The PUMA library spends about 1 microsecond per observation (involving computing observatory, Earth, Moon locations in the J2000 ecliptic coordinate system, etc), and  $(\rho_0, \dot{\rho}_0)$  computation (involving the orbit fit iteration described above), so a  $10 \times 10$  grid initialization on 4 observations followed by a Levenberg-Marquard least squares fit completes in less than a millisecond.

The accuracy of the PUMA extrapolation can be demonstrated using a near Earth asteroid 2012 KF47 which passed by the Earth near the end of Feb 2022. ATLAS observed this NEO from all four observatories for two weeks during which its distance  $\rho$  changed from 0.24 AU to 0.29 AU, its radial velocity component  $\dot{\rho}$  changed from +1.8 km/s to +6.9 km/s, and its tangential velocity changed from 1.30 deg/day to 1.33 deg/day to 1.11 deg/day.

Downloading the exact ephemerides for 2012 KF47 from JPL Horizons<sup>5</sup>, we do a PUMA fit to a short arc of 4 RA and Dec points spanning 0.9 hour on MJD 59609 using the precise JPL Horizons RA and Dec coordinates. (We chose this particular MJD because the angular velocity has a substantial acceleration at that moment of the passage.) The result is that the error in the PUMA calculated RA grows quadratically with time at a rate of  $-9$  arcsec/day<sup>2</sup> and the Dec error is  $+12$  arcsec/day<sup>2</sup>. The PUMA derived distance is smaller than true distance by 2.6%, and the fitted radial velocity is 32% smaller than the true velocity.

If we instead present PUMA with 4 points that span the same 0.9 hour on MJD 59609 and an additional 4 points spanning 0.9 hour one day later, the PUMA fit differs from JPL Horizons by only 0.03 arcsec in RA and 0.01 arcsec in Dec after a span of 20 days. The PUMA fit distance is 0.5% smaller than the true distance and the radial velocity is 16% larger than the true velocity.

The reason for the improvement with 8 points over a longer time span is that PUMA’s polynomial approximations to the gravitational acceleration and angular motion can be misled when PUMA only sees a very short arc for an object such as 2012 KF47 which in fact has substantial angular acceleration. Based on a time span of only 0.9 hour, the angular velocity that goes into Eq 6 is unrepresentative enough that the centrifugal contribution to  $\ddot{\rho}$  creates this quadratically growing error in the along-track extrapolation. When PUMA is given 8 points that span a  $\delta t$  that is about 50 times longer the error from the centrifugal contribution becomes negligible. For any asteroid whose angular velocity is changing linearly with time the 0.9 hour arc would have been sufficient to achieve this  $\sim 30$  milliarcsec accuracy.

This particular PUMA calculation took 0.4 millisecc for 8 points, if we dispense with an initial grid search, including the non-linear least squares fit for the distance and radial velocity, or 3 millisecc with 8 points if we ask for a full grid search to be sure of good initial conditions (the result is the same).

<sup>5</sup> <https://ssd.jpl.nasa.gov/horizons>



During the presentation below of PUMALINK we describe more examples of PUMA performance on very nearby asteroids, and we distribute other examples with our source code, including an impactor and the Tesla roadster. The PUMALINK tests run PUMA on billions of cases, and the resulting  $\chi^2_\nu$  values for real objects demonstrate that PUMA robustly produces orbits consistent with observations for a very wide variety of input data.

Two other orbit fitters in common use are “`openorb`” (Granvik et al. 2009) and Bill Gray’s “`Find_Orb`”<sup>6</sup>. Using each of these to fit an orbit to these same points took about 10 sec for `openorb` and 0.1 sec to 0.3 sec for `Find_Orb`. These two packages are more sophisticated than the PUMA library in terms of number of perturbers in the Solar System, integration accuracy, allowable span between data points, etc, but the PUMA library excels at raw speed with enough accuracy for any linking problem.

It is important to keep in mind that the PUMA library is fitting the points it is given, and its interpolation among these points is accurate at the 10’s of milliarcsec level. Although PUMA is remarkably accurate when asked to extrapolate beyond its data points, it is evaluating a shrewdly chosen set of polynomials and not actually doing an exact differential equation integration with the usual acceleration evaluations and predictor-corrector iterations. Therefore PUMA’s accuracy will degrade with extrapolation times  $\Delta t$  that are more than  $\sim 1000$  the inter-observation time  $\delta t$  or extrapolations over a time span during which the Earth’s orbit deviates significantly from a polynomial. On the other hand, PUMA is explicitly using the gravity of the Sun, Earth, and Moon, so its accuracy does not erode because an object is near the Earth.

### 3. LINKING

The previous section illustrates how to determine a distance and radial velocity from three or more observations, or, given a distance and radial velocity, how to project a pair of observations to a different ephemeris time. The object’s motion relative to the Earth-Moon barycenter is smooth and well described by a polynomial approximation for the acceleration it feels, so the results returned by PUMA are accurate at the observational uncertainty level for at least a month.

In this section we will examine how to decide whether linked pairs or sets of observations (“tracklets”) taken at very different times should be tested against one another with PUMA. Since it takes of order 1 millisecond to do an accurate PUMA test we easily can afford to perform  $10^5$  PUMA tests per observation, but  $10^7$  or  $10^8$  tests becomes excessively expensive so we cannot blindly test all pairs of tracklets. Our goal is to find a way to determine whether two tracklets *cannot* link, with a compute time less than 1 microsecond, so the remaining possibilities can be passed on to PUMA for a more rigorous test.

There are two sources of uncertainty when comparing two tracklets at very different times. The first is simply the statistical uncertainty that arises from the astrometric uncertainty of each detection. This is typically a fraction of an arcsecond at the moment of detection, depending on SNR, but of course it grows with extrapolation in time. The second uncertainty arises because the detections that comprise a tracklet could be at any distance and radial velocity.

In this section we will examine how the statistical uncertainty propagates in time, then the effects of distance and radial velocity uncertainty, and finally a fast method to compare pairs of tracklets.

#### 3.1. Propagation of measurement uncertainty

Given a linked pair of detections, and we want to know where an object creating these detections will be found at a different time. Given coordinates  $\mathbf{p}_1$  and  $\mathbf{p}_2$  with uncertainties  $\sigma_1$  and  $\sigma_2$ , separated by a time interval  $\delta t$ , we assign an initial position and velocity

$$\begin{aligned}\mathbf{p}_0 &= [\mathbf{p}_1/\sigma_1^2 + \mathbf{p}_2/\sigma_2^2] [1/\sigma_1^2 + 1/\sigma_2^2]^{-1} \\ \mathbf{v}_0 &= (\mathbf{p}_2 - \mathbf{p}_1)/\delta t.\end{aligned}$$

The uncertainty in the tracklet components is

$$\begin{aligned}\langle p_0^2 \rangle &= [1/\sigma_1^2 + 1/\sigma_2^2]^{-1} \\ \langle p_0 v_0 \rangle &= 0 \\ \langle v_0^2 \rangle &= (\sigma_1^2 + \sigma_2^2)/\delta t^2.\end{aligned}$$

<sup>6</sup> [https://www.projectpluto.com/find\\_orb.htm](https://www.projectpluto.com/find_orb.htm)

assuming  $\mathbf{p}_1$  and  $\mathbf{p}_2$  are uncorrelated. (The averaging indicated by  $\langle \rangle$  is understood to be relative to the mean values.) Assuming unaccelerated evolution, propagating this tracklet by time  $\Delta t$  gives

$$\begin{aligned}\mathbf{p}(t) &= \mathbf{p}_0 + \mathbf{v}_0 \Delta t \\ \mathbf{v}(t) &= \mathbf{v}_0.\end{aligned}$$

The uncertainty in the tracklet after an interval  $\Delta t$  is

$$\begin{aligned}\langle p^2 \rangle &= \langle p_0^2 \rangle + \langle v_0^2 \rangle \Delta t^2 = [1/\sigma_1^2 + 1/\sigma_2^2]^{-1} + (\sigma_1^2 + \sigma_2^2) \Delta t^2 / \delta t^2 \\ \langle pv \rangle &= \langle v_0^2 \rangle \Delta t = (\sigma_1^2 + \sigma_2^2) \Delta t / \delta t^2 \\ \langle v^2 \rangle &= \langle v_0^2 \rangle = (\sigma_1^2 + \sigma_2^2) / \delta t^2.\end{aligned}$$

As an illustration, if  $\sigma_1 = \sigma_2 = \sigma$  we get for a covariance matrix for  $p, v$  after interval  $\Delta t \gg \delta t$

$$\mathbf{C} = \frac{2\sigma^2}{\delta t^2} \begin{pmatrix} \Delta t^2 + \delta t^2/4 & \Delta t \\ \Delta t & 1 \end{pmatrix}, \quad (13)$$

and inverse covariance matrix

$$\mathbf{C}^{-1} = \frac{2}{\sigma^2} \begin{pmatrix} 1 & -\Delta t \\ -\Delta t & \Delta t^2 + \delta t^2/4 \end{pmatrix}. \quad (14)$$

Note that the determinant of  $\mathbf{C}$  is completely independent of time  $\Delta t$ : the  $p, v$  astrometric uncertainty volume just squeezes out into an ever thinner line even though the uncertainty on  $p$  individually grows linearly with  $\Delta t$ .

If  $\mathbf{p}$  comprises two uncorrelated coordinates such as unit tracklet components or angle on the sky, the 6D or 4D covariance matrix consists of  $2 \times 2$  blocks for the displacement and velocity in each coordinate. If the uncertainties in these coordinates are correlated, for example because the along-track error is different from the cross-track error, the covariance matrix is more complicated.

### 3.2. Influence of $\rho, \dot{\rho}$ on tracklet propagation

Suppose for the moment that an object has no acceleration relative to the usual Earth-Moon barycenter origin and moves at constant velocity. Two angular observations on the sky, augmented by an assumption about distance and radial velocity, allow us to calculate the trajectory of this object.

Referring again to Fig 1, suppose we have two observations at  $t_0$  and  $t_1$  (dropping the primes for clarity) with time interval  $\delta t = t_1 - t_0$ , of an object that is moving at constant velocity relative to the Earth-Moon barycenter. We want to know where it is after at a reference time  $\Delta t$  after  $t_0$ . If we assume that the object has a distance and radial velocity of  $\rho, \dot{\rho}$  at this reference time, we can linearly extrapolate the two earlier observations to get the 3D object position  $\mathbf{x}$  relative to the barycenter origin.

We divide by this result by  $\rho$  to get the extrapolated unit vector at that time. To second order in  $1/\rho$ , and taking  $\delta t \ll \Delta t$ ,

$$\begin{aligned}\frac{1}{\rho} \mathbf{x}(\Delta t) &\approx \hat{\mathbf{u}}_0 + \Delta t \dot{\boldsymbol{\varphi}} \\ &+ \frac{1}{\rho} \left[ -\dot{\rho} \Delta t^2 \dot{\boldsymbol{\varphi}} + \dot{\mathbf{D}} \Delta t + \mathbf{D}'_0 - D_{\parallel} (\hat{\mathbf{u}}_0 + \Delta t \dot{\boldsymbol{\varphi}}) \right] \\ &- \frac{1}{2\rho^2} \left[ (D_{\perp}^2 + \dot{\rho}^2 \Delta t^2) \Delta t \dot{\boldsymbol{\varphi}} + (D_{\perp}^2 - \dot{\rho}^2 \Delta t^2) \hat{\mathbf{u}}_0 \right],\end{aligned} \quad (15)$$

where the observed tangential motion of the object and observatory motion are defined as

$$\dot{\boldsymbol{\varphi}} \equiv \frac{1}{\delta t} (\hat{\mathbf{u}}_1 - \hat{\mathbf{u}}_0), \quad \dot{\mathbf{D}} \equiv \frac{1}{\delta t} (\mathbf{D}'_1 - \mathbf{D}'_0),$$

and  $D_{\perp}$  and  $D_{\parallel}$  are the perpendicular and parallel components of  $\mathbf{D}'_0$  with respect to  $\hat{\mathbf{u}}_0$  as above. Equation 15 may be differentiated with respect to  $\Delta t$  to get the extrapolated angular velocity.

Note that if  $D \sim R_{\oplus}$  and  $\rho \sim 1$  AU,  $D/\rho$  is  $\sim 4 \times 10^{-5}$ ,  $\dot{D}\Delta t/\rho$  is  $\sim 2 \times 10^{-3}$  over  $\Delta t \sim 10$  days, and  $\dot{\rho}$  is an order of magnitude bigger than  $\dot{D}$  for typical orbital velocities. Therefore the terms involving  $D$  make a small contribution in Eq 15.

This is the motivation for computing the motion relative to the Earth-Moon barycenter, as close to the observations as possible without incurring rapid wiggles in inertial space. HeliLinC, using a the Sun as the origin with  $D \sim 1$  AU, computes a motion that is quite sensitive to the choice of the (unknown)  $\rho, \dot{\rho}$ , and the following analytic progress is impossible unless  $\rho \gtrsim 1$  AU.

Define  $s$  as the inverse distance, and  $w$  as the inverse of the ‘‘collision time’’, before a radially moving object will arrive at the Earth:

$$s \equiv \frac{1}{\rho} \quad \text{and} \quad w \equiv \frac{\dot{\rho}}{\rho}.$$

(These variables  $s$  and  $w$  are almost exactly the same as  $\gamma$  and  $\dot{\gamma}$  used by Bernstein & Khushalani (2000) and Holman et al. (2018), but the different origins make the variables slightly different. These origin differences are in fact critical, the use of dimensional  $\gamma$  and  $\dot{\gamma}$  along with their dimensionless  $\alpha$  and  $\beta$  can be confusing, and PUMA explicitly avoids spherical coordinates. We deem it advisable therefore not to reuse these variable names from the literature.)

Neglecting terms proportional to  $D$ , we can rewrite Equation 15 in terms of the variables  $s$  and  $w$ ,

$$\frac{1}{\rho} \mathbf{x}(\Delta t) \approx \left[ \frac{3}{2} - \frac{(1 + w\Delta t)^2}{2} \right] \Delta t \dot{\boldsymbol{\varphi}} + \left[ 1 + \frac{(w\Delta t)^2}{2} \right] \hat{\mathbf{u}}_0 + \dot{\mathbf{D}} \Delta t s. \quad (16)$$

The term  $w\Delta t$ , the ratio between extrapolation time and collision time, is typically small unless impact is imminent, so its square is smaller still:

$$w\Delta t = \frac{\dot{\rho}}{\rho} \Delta t = 0.06 \left( \frac{\dot{\rho}}{10 \text{ km/s}} \right) \left( \frac{\rho}{0.1 \text{ AU}} \right)^{-1} \left( \frac{\Delta t}{1 \text{ day}} \right). \quad (17)$$

Of course a proper PUMA extrapolation neglects neither  $D$  nor the accelerated motion of the object with respect to the barycenter, but these only modify the exact polynomial coefficients and do not fundamentally change the linear behavior for  $|w\Delta t| \ll 1$ .

This implies that each component of the extrapolated unit vector and extrapolated velocity divided by distance from a pair of observations spans a triangle in 6D space, with vertices at  $\rho = \infty$  and the minimum and maximum plausible  $\dot{\rho}$  at the minimum  $\rho$  considered. Using PUMA to accurately extrapolate the observations with a test set of  $\rho_0, \dot{\rho}_0$  to the reference time, a planar fit to each of these coordinates as a function of the resulting  $s, w$  is very accurate when  $|w\Delta t| \ll 1$ .

That the manifold of possible extrapolations in 6D phase space for a pair of observations is 2 dimensional is not surprising, given that it is determined by the unknown  $\rho, \dot{\rho}$ , but it is a nice surprise that it is a nearly planar triangle and nearly linear in  $s, w$ . The size of the triangle and extent of uncertainty depends on the minimum value of  $\rho$  and maximum absolute  $\dot{\rho}$  according to  $|w\Delta t|$ , so the computer resources can be tailored according to how close the user wants to approach impact time. Section 3.4 provides some illustration of these triangles

Venturing to very small  $\rho$  will increase  $w$ , make  $|w\Delta t| \sim 1$ , and cause non-linear terms such as  $w^2$ ,  $sw$ , and  $s^2$  to become significant. (Although the position does not have  $sw$  and  $s^2$  terms, the velocity does.) By restricting  $w\Delta t$  to the linear regime, we can exploit this approximation to test the linkage between observations very quickly over a wide range of  $\rho, \dot{\rho}$ .

### 3.3. Linking two pairs of observation

We now have the ingredients to test whether two pairs of observations taken at time  $t_1$  and  $t_2$  might link with one another. We start by picking a common reference time when they can be compared. Because there are terms that depend on  $\Delta t^2$  and because the validity of the linear approximation of the previous section depends on  $|w\Delta t| \ll 1$  it is advantageous to choose an comparison time that makes  $|\Delta t_1|$  and  $|\Delta t_2|$  as small as possible, for example half way between  $t_1$  and  $t_2$ .

The results of the previous section allow us to calculate the unit vector and distance divided velocity of each of these tracklets at this reference time, expressing the result as a polynomial in the unknown  $s, w$  distance and radial velocity at the reference time.

For a choice of  $\rho, \dot{\rho}$  (i.e.  $s, w$ ) designate  $\mathbf{S}_1(s, w)$  and  $\mathbf{S}_2(s, w)$  as the distance-divided 6D state vectors at the reference time for the two tracklets: these are each polynomials in  $s, w$  where the fit to the trial values propagated using PUMA gives us all the coefficients. We can also assemble the 6D covariance matrices  $\mathbf{C}_1$  and  $\mathbf{C}_2$ , which we take to comprise three  $2 \times 2$  blocks for each coordinate as described in Eq 13 above. We assume that  $\mathbf{C}_1$  and  $\mathbf{C}_2$  do not depend on  $s, w$ , but we do augment them by the covariance matrix from the errors of the linear fit with respect to the grid of points that produce the coefficients for  $\mathbf{S}_1$  and  $\mathbf{S}_2$ .

Then the simultaneous statistical compatibility of some arbitrary state vector  $\mathbf{S}$  with  $\mathbf{S}_1(s, w)$  and  $\mathbf{S}_2(s, w)$  is governed by

$$\chi^2(s, w) = (\mathbf{S} - \mathbf{S}_1)^T \mathbf{C}_1^{-1} (\mathbf{S} - \mathbf{S}_1) + (\mathbf{S} - \mathbf{S}_2)^T \mathbf{C}_2^{-1} (\mathbf{S} - \mathbf{S}_2). \quad (18)$$

We are seeking a solution such that  $\mathbf{S}_1$  and  $\mathbf{S}_2$  are evaluated at the same  $s, w$ ; therefore since  $\mathbf{S}_1$  and  $\mathbf{S}_2$  are polynomials of  $s, w$ ,  $\chi^2(s, w)$  is also a polynomial of  $s, w$ .

Taking the derivative with respect to  $\mathbf{S}$ , the minimum of  $\chi^2$  occurs at the inverse variance weighted average of the two locations

$$\mathbf{S}_{min}(s, w) = \mathbf{C} (\mathbf{C}_1^{-1} \mathbf{S}_1 + \mathbf{C}_2^{-1} \mathbf{S}_2), \quad (19)$$

where the combined inverse covariance matrix is the sum of the two matrices from the two tracklets

$$\mathbf{C}^{-1} = \mathbf{C}_1^{-1} + \mathbf{C}_2^{-1}. \quad (20)$$

Eq 19 is linear in  $\mathbf{S}_1(s, w)$  and  $\mathbf{S}_2(s, w)$ , so the most statistically likely  $\mathbf{S}_{min}(s, w)$  is also a polynomial in  $s, w$  of the same order. Plugging this result back into Eq 18 yields an expression for  $\chi^2$ , which has polynomial terms from the matrix squares of  $(\mathbf{S}_{min} - \mathbf{S}_1)$  and  $(\mathbf{S}_{min} - \mathbf{S}_2)$ . This expression for  $\chi^2$  is therefore now quadratic in  $s, w$ , with coefficients multiplying  $1, s, w, w^2, sw,$  and  $s^2$ . (A quadratic fit to  $\mathbf{S}_1, \mathbf{S}_2$  leads to a quartic  $\chi^2$  and 15 coefficients.)

An expression for  $\chi^2(s, w)$  that is quadratic in  $s, w$  can be cast in the form:

$$\chi^2(s, w) = \chi_0^2 + e_1(s - s_0)^2 + e_2(s - s_0)(w - w_0) + e_3(w - w_0)^2. \quad (21)$$

The statistically most compatible distance and radial velocity are evident as  $s_0, w_0$ , and the minimum value of  $\chi^2(s, w)$  emerges as  $\chi_0^2$ . The contours in  $\chi^2$  are nested ellipses whose size and orientation is given by the coefficients  $e_1, e_2$ , and  $e_3$ , and these can be converted to uncertainties and covariance in  $s_0$  and  $w_0$ .

Note that if we kept the quadratic terms for the fits to  $\mathbf{S}_1$  and  $\mathbf{S}_2$  it would not fundamentally change this approach. Finding the best fit  $\mathbf{S}_{min}$  and evaluating the  $s, w$  that minimize  $\chi^2$  simply involves finding roots of higher order polynomials, or more realistically, treating the quadratic terms as perturbations on the linear function and adjusting the result accordingly. The current implementation is sufficiently accurate without the quadratic terms.

### 3.4. A NEO example

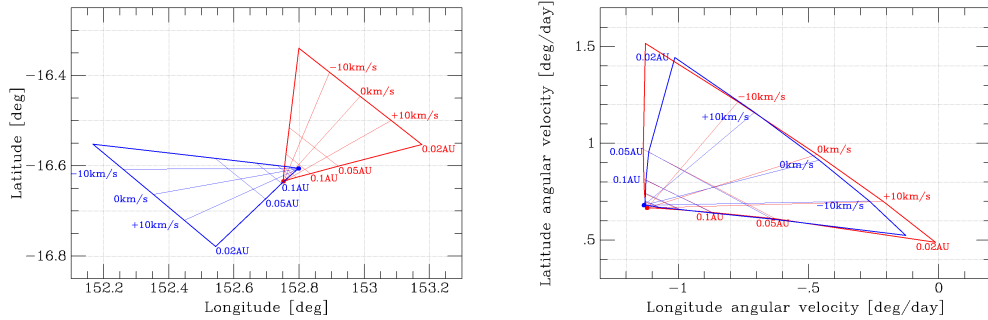
Returning to the NEO 2012 KF47 that ATLAS observed in Feb 2022 at  $\rho$  of 0.24 AU to 0.29 AU and  $\dot{\rho}$  of +1.8 km/s to +6.9 km/s, we can examine how PUMALINK uses a pair of detections from two different nights to determine whether the two tracklets link with one another.

Figure 2 shows the PUMA prediction for where this NEO would be, as seen from the Earth-Moon barycenter, at MJD 59607.0, given tracklets taken from 59606.47 and 59607.53. This calculation shows only the effect of  $\rho, \dot{\rho}$  without taking observational errors into account. The triangle vertices near ecliptic longitude 152.8 and latitude  $-16.6$  that correspond to great circle extrapolation are offset by about 0.05 degree because the object is in fact not infinitely far away; it is 0.242 AU distant at that time. These two tracklets are consistent with one another if they match in all four dimensions at the same  $s, w$ .

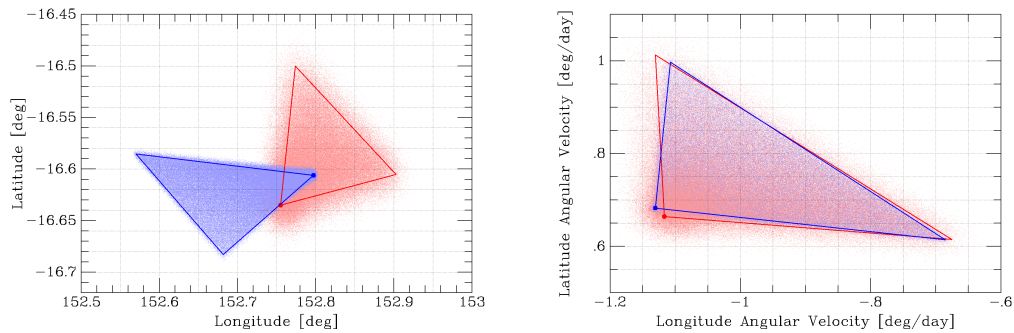
Figure 3 shows a subregion from Fig 2 with the scatter possible from observational uncertainties applied as well. This fuzzes out the triangles, and it implies that the two tracklets do not need to match exactly at the same  $s, w$  in order to be statistically consistent. Note that the uncertainty in where the asteroid lies caused by uncertainty in  $\rho, \dot{\rho}$  is considerably bigger than the astrometric uncertainty at distances smaller than 0.2 AU.

Figure 4 repeats figure Fig 3, but statistically scattered points are only shown for a particular  $\rho, \dot{\rho}$ , set to be the actual values for 2012 KF47.

Recall that the 4D uncertainty volume is actually very small, however. Figure 4 demonstrates that although consideration of only a positional match or velocity match bears a lot of uncertainty, a proper consideration of the covariance



**Figure 2.** The NEO 2012 KF47 was observed by ATLAS on MJD 59606.47 and 59607.53. The left panel shows the extrapolated barycenter position for pairs of detections from each night at the intermediate MJD 59607.0 for a variety of assumptions for  $\rho, \dot{\rho}$  at that reference time, and the right panel shows the extrapolated angular velocity. The extrapolation of the pair from the first epoch forward is shown in red, the extrapolation of the pair from the second epoch backward is shown in blue, and labels show selected values of  $\rho, \dot{\rho}$ . A viable solution can only exist for an overlap in these four coordinates at a common value of  $\rho, \dot{\rho}$ . The dots on one vertex of the triangles show the great circle extrapolation for  $\rho$  infinitely far away.



**Figure 3.** This figure shows similar calculations for NEO 2012 KF47 as Fig 2 but expanded to show only a minimum distance of 0.05 AU and  $\pm 20$  km/s at the observational epochs, this time including random variations in all four observations. The left panel shows the effect in position–position space, the right is velocity–velocity space. The point at infinity is marked with a dot on the bounding triangles. The scatter for the first (red) epoch is greater because  $\delta t$  is 834 sec, compared with 3978 sec for the second (blue) epoch.

between position and velocity in each coordinate is very restrictive on whether two tracklets are statistically consistent with one another. The linear fit as a function of  $s, w$  to the points seen in Fig 3 has an RMS error of 2.5 arcsec in angular coordinate and 12 arcsec/day in angular velocity

### 3.5. Software implementation

We have implemented these algorithms in a program called “PUMALINK”. The processing follows a number of steps, illustrated in Fig 5, and detailed below. The only requirement for the user is to organize a set of detections into “TRD9” format, which is MJD, RA, Dec, cross-track astrometric error, along-track astrometric error, observatory longitude, latitude, and elevation, and an arbitrary, unique string ID. PUMALINK works by organizing pairs of detections within an epoch into tracklets and then linking pairs of tracklets from two epochs into a quad. The user should be mindful of this to ensure that PUMALINK will join detections into tracklets and identify the two different epochs properly.

These are the PUMALINK steps.

- Read a set of detections in “TRD9” format.
- Link these detections into tracklets, using different options: by default PUMALINK internally links pairs of detections within a limiting time ( $\text{dtmax}$ , default 0.1 day) and angular velocity ( $\text{omega}$ , default 5 deg/day), but PUMALINK can also use externally provided tracklets designated using the detection IDs.

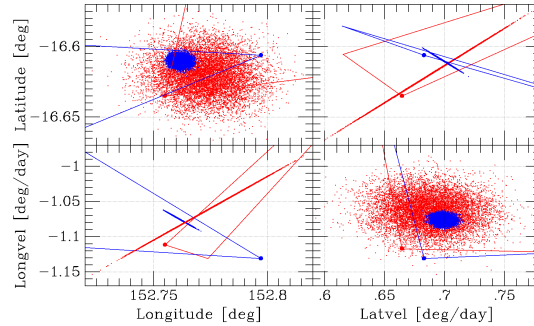


**Figure 4.** The triangles that show the range of possibility for the location of the NEO 2012 KF47 caused by variation in  $\rho, \dot{\rho}$  are expanded again from Fig 3. In this figure the scatter caused by error in observational error is restricted to the correct  $\rho, \dot{\rho}$  of 0.242 AU, +2.04 km/s at 59607.0. The upper left panel shows the scatter in the position–position plane, the lower left panel is longitude position–longitude velocity (latitude is in the upper right), and the lower right panel is the velocity–velocity plane (axes flipped with respect to Fig 3). As before the two epochs are indicated by red and blue. At a fixed  $\rho, \dot{\rho}$  the 4D observational scatter is a very thin disk that has a significant spread in position–position and velocity–velocity, but whose thickness in the position–velocity planes is comparable to the observational astrometric uncertainty.

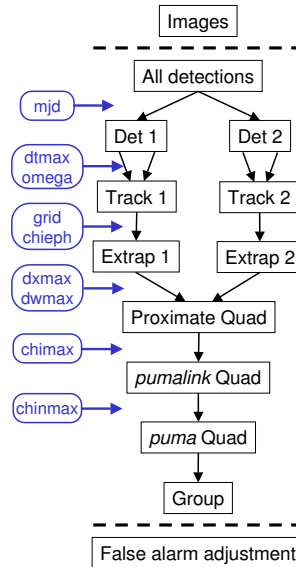


**Figure 5.** The processing flow of PUMALINK starts after a set of images have been processed to produce a set of detections, and after PUMALINK completes the user must choose where to set the thresholds for detection probability versus false alarm rate.

- Use the PUMA library to extrapolate each tracklet to the reference time (`mjd`, normally taken to be the midpoint of the biggest time gap between detection times). This is computed for a grid of possible distances and radial velocities, by default 5 steps in distance from 0.02 AU to 4 AU and 5 steps in velocity from  $-20$  km/s to  $+20$  km/s. The results in each of the 6 unit vector and distance divided velocity components are fitted as a linear function of  $s, w$ , saving the coefficients and covariance matrix between each component’s position and velocity with respect to the fit.
- Use a 6D kd-tree to find all pairs of tracklets that are sufficiently close at the reference time to bear further examination, nominally with search dimensions of `dxmax` 0.2 deg and `dwmax` 0.5 deg/day. These associated tracklets create a proximate quad.

- Apply the link testing algorithm described above to evaluate the minimum  $\chi^2(s, w)$ . If  $\chi_{min}^2$  is sufficiently small (nominally `chimax` < 25) continue consideration of this pair of tracklets. The covariance matrices include both the projected uncertainties from Eq 13 added to the covariance from the linear fit to the extrapolation grid in  $s, w$ .
- Perform a PUMA fit to all the detections from the pair of tracklets. If the PUMA reduced  $\chi_\nu^2$  is sufficiently small (nominally `chinmax` < 25) record this pair of tracklets as a “quad”. (A quad has 4 detections when PUMALINK creates tracklets from internally linked pairs of detections.) Also compute the probability that the detections from this quad arise from one ( $\chi_{\nu_s}^2$ ) or two ( $\chi_{\nu_d}^2$ ) stationary objects. (PUMALINK treats stationary transients as moving objects with zero angular velocity, and  $\chi_{\nu_s}^2$  permits odds testing between stationary and moving hypotheses.)
- Once PUMALINK has tested all pairs of tracklets and assembled all quads, PUMALINK groups all quads according to whether they share a detection with some other quad in the group: different groups have no detection in common. Within each detection group PUMALINK examines the result of the PUMA fit to each quad at the reference time, and groups all quads which are very close to one another (nominally 0.01 deg and 0.002 deg/day). Quads which are close but have inconsistent detections from a single epoch are not allowed to group, so a mis-linkages are not allowed to group with correct linkages. The detections from singleton quads and groups that are subgroups of a larger group are dissolved into the bigger group.
- A final PUMA fit using the detections from each group with more than 4 detections is recorded.
- PUMALINK writes the results for each individual quad and the aggregate results from each quad group. The detections that make up each quad or group are written as a comma separated list which may be used as a tracklet designation for a future run of PUMALINK. Note that the fundamental output from PUMALINK is the file with individual quads because groups with more than 4 detections can only exist for applications that have more than 2 detections per epoch.

We desire three features of any linkage procedure: 1) high probability of identifying correct linkages, 2) speed of execution, and 3) low number of false linkages relative to good ones.

PUMALINK prioritizes these three features in order. For false alarms, the PUMA values of  $\chi_\nu^2$  for the hypothesis of asteroid orbit and the  $\chi_{\nu_s}^2$  and  $\chi_{\nu_d}^2$  values testing a mis-linkage of one or two stationary objects provide a probability that a linking is correct or not.  $\chi^2$  has a distribution of  $\frac{1}{2} \exp(-\frac{1}{2}\chi^2)$  for  $N = 8 - 6 = 2$  degrees of freedom for a quad, so the nominal threshold of  $\chi_\nu^2 < 25$  will pass many false alarms into the output file that need to be rejected by the user.

The choice of parameter thresholds by the user may be used to trade completeness against execution speed, and the best choice depends on the input data. PUMALINK is most sensitive to two dimensionless numbers from the data:  $\Delta t/\delta t$ , the ratio of extrapolation interval to intra-tracklet interval, and  $w\Delta t$ , the ratio of the extrapolation time and the notional “collision time”. When  $\Delta t/\delta t \gg 200$  it may be necessary to widen the tolerances for the kd-tree first association of tracklets. When  $w\Delta t$  approaches 1 the linearity approximation degrades and it may be necessary to increase the kd-tree search tolerances or else limit the extrapolation grid away from very small values of  $\rho$  or very large values for  $|\dot{\rho}|$  which make  $w$  large. Of course, PUMALINK can be run multiple times with different extrapolation grid ranges, for example 0.1–4 AU and 0.01–0.1 AU.

Obviously the number of input detections and the limiting angular velocity for forming tracklets affects the execution speed. For many datasets the execution time for PUMALINK is dominated by the tracklet extrapolation stage, which takes approximately 150 microseconds per tracklet. The number of tracklets goes as the square of the product of the number of detections, the limiting angular velocity, and the typical intra-tracklet interval. For typical sky surveys the number of tracklets is roughly in the range  $N_{track} \sim 10^{-5} N_{det}^2$ , so the PUMALINK execution time is roughly 1–100 nanosec per  $N_{det}^2$ .

### 3.6. Pumalink performance

We performed a number of tests of PUMALINK on a variety of datasets that illustrate its performance. The first test is a set of normal ATLAS operations from MJD 58995 to 59005 (new to full moon), the second test is a set of special ATLAS observations with 110 sec exposures of a particular field near opposition from MJD 59991 to 60003 (last to first quarter moon), and the last test was an LSST simulation kindly provided by Ari Heinze and Mario Juric spanning future MJD 60601 to 60616 (full to new moon).

ATLAS carefully notes the presence of all known asteroids (“kast”) for each exposure, and the completeness of known asteroids is very high at the ATLAS limiting magnitude, so the kasts allow us to evaluate object detection probability and false alarm rates.

### 3.6.1. ATLAS nights

From MJD 58995 to 59005 the two Hawaii observatories stepped between four declination bands, Maunaloa and Haleakala following each other so each band was observed every other day. Each field was nominally targeted 4 times on each night, and the time intervals  $dt$  between successive observations were approximately 5, 15, and 30 min. We ran PUMALINK on each night against every other night that covered the same Dec band, so the lag times spanned by the two PUMALINK epochs were 2, 4, 6, 8, and 10 days. We made no attempt to condense the 4 visits to each field every night directly, and simply let PUMALINK deal with all possible pairs of detections for each object. ATLAS detections are each tested by up to five different functions depending on SNR: fixed PSF, adjustable PSF, trailed PSF, long streak PSF, and negative flux, and then a preliminary classification for each detection assigns it to one of 8 possibilities, of which one corresponds to a real object that is not a variable star. Detections were excluded if this basic ATLAS classifier probability of being real was lower than 10%, or if they were output from the routines that fit trailed detections.

The 21 declination band visits created 45 overlapping pairs of nights, the median number of detections given to PUMALINK for a pair of nights was 2.5M, the median number of tracklets formed was 10M, and the median execution time was 1800 sec (1 core, 3GHz). We deem a kast to be “linkable” by PUMALINK when at least two detections exist for it from each epoch so that two tracklets may be formed. Among the pairs of nights, the median fraction of kast actually found by PUMALINK was 98.7%. This success fraction drops quadratically as a function of lag time between nights, changing from 99.7% at a lag of 2 days to 94.5% at a lag of 8 days. Overall, of the 32859 kasts that were linkable between a pair of nights, PUMALINK found 32585, 99.2%.

To quantify the performance we use a binary confusion matrix where TP and TN designate correct classifications of actual positive and negative cases as positive and negative, and FN and FP are erroneous classifications of actual positive and negative objects as negative or positive. A FN (“miss”) counts against the detection probability and a FP adds to the false alarm rate.

We calculate a “probability of detection” (PD, also known as “recall”) as the fraction of all linkable kasts that appear in at least one quad, i.e.  $TP/(TP+FN)$ . The number of TN is ill-defined and potentially vast, so we define our “false alarm rate” (FAR) as the fraction of all quads which do not match any kast or which mis-link different kasts, i.e.  $FP/(TP+FP)$ . This is also known as  $(1-\text{“precision”})$ .

As noted above, the performance depends on the lag time  $\sim 2\Delta t$  between pairs of nights for the nominal parameters. Of course the PD and FAR depend on many different input parameters, but it is illustrative to vary only the PUMA  $\chi^2_\nu$  threshold for keeping a linkage and generate the set of curves of PD and FAR illustrated in Figure 6.

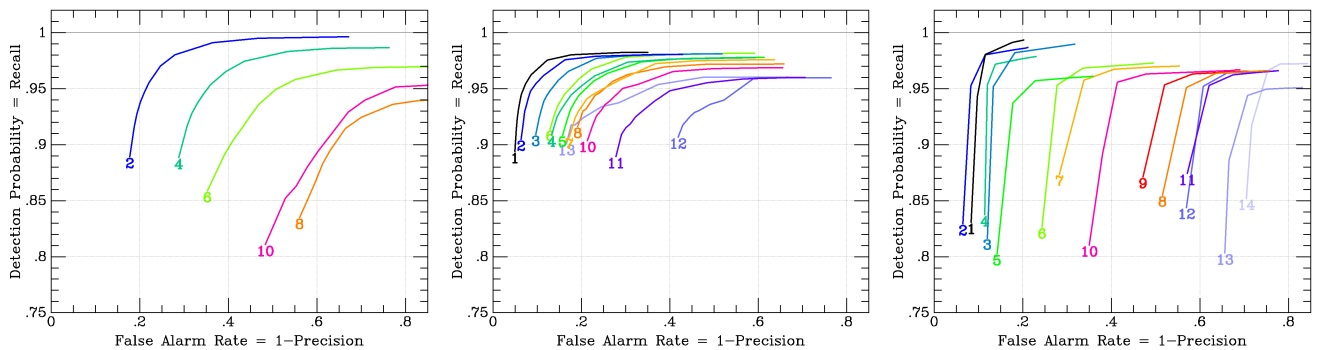


**Figure 6.** This figure shows the detection probability versus false alarm rate (“receiver operating characteristic” or ROC curve) for the performance of PUMALINK on the three datasets as a function of the  $\text{chinmax } \chi^2_\nu$  threshold parameter. The left panel shows the 11 full ATLAS nights, the middle panel the ATLAS opposition field experiment, and the right panel the LSST simulation. For these “detection probability” is the fraction of all linkable kasts that are linked by at least one quad and the “false alarm rate” is the fraction of all quads that do not associate with any kast. The colors and labels show the inter-epoch lag time: black through magenta are lags from 1 to 10 days, then lighter shades of purple show lags to 14 days for the opposition and LSST tests.



This experiment has  $\Delta t/\delta t$  as large as  $\sim 1500$ , which causes the PD and FAR performance to degrade for the biggest lags. Opening up the tolerance for the kd-tree linkage could recover some of this performance at the cost of more compute time and FAR.

Although the PD reaches very respectable values, the FAR is never very small for this full night test. An extrapolation by  $\Delta t/\delta t \sim 100$  or larger will always admit false linkages that are statistically reasonable. However, a 50% false alarm rate is actually very manageable. Each candidate linkage typically is subjected to additional image scrutiny (human or machine), and there are other statistics that can be considered, even from PUMALINK (such as  $\chi_s^2$  and  $\chi_d^2$ , or using a process of elimination on detections to reject mis-linked quads). Removal of false alarms (potentially at the cost of real detections) depends on the application and is beyond the scope of what PUMALINK can do by itself, but we discuss FAR reductions strategies in the next section.

Figure 6 treats each pair of epochs separately, and combining the linkages from multiple pairs of nights does improve the PD and suppress the FAR. In addition, given more than two epochs PUMALINK can be run hierarchically, taking advantage of the performance at small lag time before running PUMALINK over a bigger lag time using the output linkages from a previous iteration.

The distribution of the magnitudes of the linked kasts peaks at  $V \sim 18.6$  and the 50% detection rate occurs at  $V \sim 19.0$ . The nearest kast found by PUMALINK with the default parameters during this exercise was at 0.30 AU and the fastest was 2.7 deg/day. NEO 513170 was also present in these observations at 0.11 AU and 4.3 deg/day. Although this NEO was missed by the nominal values for the kd-tree search of 0.2 deg and 0.5 deg/day, it was found when these were increased to 0.3 deg and 1.0 deg/day. Increasing these limits also increased the execution time by about 50%.

### 3.6.2. Opposition experiment

Between MJD 59990 to 60003 ATLAS observed a particular field every night fairly close to opposition so that there were many asteroids near full illumination. In addition, the exposure time was increased from 30 sec to 110 sec which increased the sensitivity by nearly a magnitude. On any given night there were 4–8 observations of the field, sometimes from different observatories. The time interval between each observation was kept uniform at  $\sim 30$  min.

These observations over 14 days created 91 pairs of nights to be compared, the median number of detections given to PUMALINK from a pair of nights was 20k, the median number of tracklets formed was 300k, and the median execution time was 35 sec. The median fraction of kast found by PUMALINK was 98.3% and the average was 97.4% but it varies less with lag time compared to the full night experiment because  $\Delta t/\delta t$  is smaller, never exceeding  $\sim 300$ , thanks to  $\delta t$  never smaller than 30 minutes.

Of the 1295 kasts which were linkable between at least two nights, PUMALINK found 1263 with the default parameters. The missing kasts mostly were ones that had a single detection from South Africa and then another from Chile 4 hours later, and that exceeds the default time difference of 0.1 day to form a pair. If that time interval between two detections to form a test tracklet is increased, PUMALINK finds 1292 of 1295 kasts, but at the cost of a higher false alarm rate.

The ROC curve seen in the middle panel of Fig 6 provides more insight into the differences between the opposition test and the full night test. The FAR at a given PD is considerably smaller for the opposition fields than for the full nights. This is the result of  $\Delta t/\delta t \lesssim 300$ : it is much less common for a false alarm linkage to be statistically consistent with the observations when the extrapolation is less extreme.

The distribution of the magnitudes of the linked kasts in these opposition fields peaks at  $V \sim 19.6$  as a result of the increase in exposure time, and the 50% detection probability occurs at  $V \sim 20.0$ . The nearest and fastest asteroid in this small opposition field was 2008CX189 (0.75 AU and 0.57 deg/day); 2008CX189 was correctly linked by PUMALINK with the nominal parameters.

### 3.6.3. LSST simulation

The Rubin Telescope<sup>7</sup> is scheduled to begin the Legacy Survey of Space and Time (LSST) sometime in 2025<sup>8</sup>. Juric et al. (2017) describe the LSST data management system, Juric et al. (2021) presents 10 year simulations of solar system moving objects appearances in the LSST data, and Heinze et al. (2022) discusses the application of HelioLinC to find these moving objects in the real data. Among the many science goals that will be addressed by LSST is the detection of large numbers of asteroids, particularly NEOs. Because the schedule will be driven by many competing

<sup>7</sup> <https://rubinobservatory.org>

<sup>8</sup> [ls.st/dates](https://ls.st/dates)

projects, the observation cadence for asteroid detection will be challenging. Nevertheless there is no doubt that the LSST will be extremely powerful, and software to analyze simulated LSST data is well advanced.

Ari Heinze and Mario Juric generously provided us with one such simulated dataset that spans future MJD 60601 to 60616. This differs from the ATLAS data already considered because there are no false alarm detections, just 5.3M detections of 995082 different asteroids with simulated astrometric error and magnitudes. Therefore “false alarm” might better be termed “mis-linkage” for this test. These detections are all labeled by an object ID (which we ignore until it is time to verify performance). We organized these into distinct observations (same exposure start time) and nights, and create detection files in TRD9 format. We assigned an astrometric error of 1 arcsec multiplied by the simulation magnitude uncertainty with 0.015 mag added in quadrature (e.g.  $\sim 0.03$  arcsec at  $m \sim 22$ ).

These 15 simulated nights make 104 pairs of epochs on which we ran PUMALINK with the nominal parameters. The median number of detections from the pairs of nights was 730k, the median number of tracklets formed from an epoch pair was 8.3M, and the median execution time for a pair of nights was 1000 sec. Of the nearly million asteroids, only 427,827 appear at least twice on two different nights and are therefore linkable by PUMALINK. Of these, the total number linked between at least two nights was 420,708, for a gross PD of 98.3%.

PUMALINK faced a number of challenges with the LSST data. Some of the  $\delta t$  intervals were extremely brief, and the extrapolation ratio of  $\Delta t/\delta t$  exceeded 12,000 for some tracklets. LSST also spends time on a number of nights observing the “deep drilling fields” which have as many as 96 exposures at the same location in a night. Our naive application of PUMALINK creates 96-choose-2 possible tracklet pairs from such a night for an asteroid in that field, and between two such nights each asteroid creates 20M different pairs of tracklets which require PUMA evaluations. Operating on such pairs of nights PUMALINK can use more than 100G of memory and 200,000 seconds to complete (although it eventually does succeed). Evidently PUMALINK could be used more efficiently with a more judicious selection of input.

The right panel of Figure 6 shows more detail on the PUMALINK performance. As with the other two experiments the PD at a given FAR and the FAR at a given PD degrade for bigger extrapolation ratios. When PUMALINK is run hierarchically, using the linkages from a pair of nights as input tracklets such as 60103–60105 and 60109–60113, the false alarm rate is zero.

The nearest and fastest linkable asteroid in the LSST simulation had ID S0000ssOa at 0.022 AU and 18.5 deg/day on MJD 60601. It is instructive to examine how PUMALINK deals with it. In the LSST simulation it also appears more than once per night on 60603 at 0.042 AU and 5.0 deg/day, on 60605 at 0.061 AU and 2.7 deg/day, on 60606 at 0.073 AU and 1.6 deg/day, on 60610 at 0.115 AU and 0.7 deg/day, and on 60611 at 0.126 AU and 0.6 deg/day. Recall that as we are running it here PUMALINK first must form a tracklet on a day within an angular velocity limit and then try to link two different days.

PUMALINK cannot form a tracklet on 60601 and 60603 with the default angular velocity of 5 deg/day, but increasing it to 6 deg/day does form a tracklet on 60603. In order for PUMALINK to link 60603 and 60605 it must be given kd-tree search limits of 1 deg and 4 deg/day instead of the defaults of 0.2 deg and 0.5 deg/day. This increased search area is necessitated by S0000ssOa’s deceleration from 5 deg/day to 1.6 deg/day over that two day time span and the limitations of PUMA’s short arc extrapolation. Between 60605 and 60606 when S0000ssOa moves from 0.06 to 0.07 AU PUMALINK needs a slightly increased search area of 0.3 deg and 0.5 deg/day. Between 60610 and 60611 PUMALINK finds S0000ssOa and links it correctly.

Once the detections for S0000ssOa are given to PUMA for testing, the result has  $\chi^2_\nu < 1$  on all pairs of nights. Of course, S0000ssOa would be trailed on the first three nights, and passing a greatly reduced set of trailed detections to PUMALINK would take negligible processing time.

The only other asteroid in the LSST set closer than 0.1 AU and moving more slowly than 5 deg/day was S0000EOMa at 0.081 AU moving at 4.41 deg/day, and it was linked by PUMALINK with the default parameters.

### 3.7. Optimizing PUMALINK and coping with false alarms

#### 3.7.1. Parameter optimization

PUMALINK can be optimized for each application by adjusting its operation parameters from the defaults. As always the optimization needs to balance the goals of high PD, low execution time, and low FAR. The three examples above illustrate how PUMALINK performs for three representative test cases with the default parameters. This optimization is application specific because PUMALINK is not witting of many survey characteristics, for example how many times a given field was observed on a given epoch or what fraction of the detections given to PUMALINK are expected to be false. This subsection will briefly describe the operating parameters and how each is likely to affect the three goals.

Given the PUMALINK results on several representative experimental datasets, we return to the discussion of Sec 3.5 illustrated in Fig 5 and offer guidance on the different parameter’s function.

- Pair formation from all the detections is governed by the parameters `dtmax` and `omega`. We saw a case with the opposition experiment where `dtmax` had to be increased to support a 6 hour time interval for a tracklet, and a case with the LSST experiment where `omega` had to be increased to 6 deg/day to find a nearby asteroid. The execution time goes approximately as the square of the product of `dtmax` and `omega`, as does the false alarm rate. For the case of very fast moving, trailed detections it is possible to set `omega` to a very large value and simply test all possible pairs with PUMALINK, at a cost of about  $\sim 10 \text{ nsec } N_{det}^2$ .
- The accuracy of the linear fit to PUMA extrapolations of tracklets is affected by the choice of the extrapolation grid. Since the predicted locations and error grows with  $s = 1/\rho$ , it is more efficient to use a minimal grid that does not extend to very small distance, but this runs the risk of not linking a very nearby object. When PUMALINK is given a user-defined set of tracklets there may not be much latitude to explore a large grid, and many of the grid points may be rejected by the PUMA extrapolation because they exceed the `chieph` parameter.
- PUMALINK sorts the extrapolated positions using a kd-tree in order to judge which tracklets should be tested with the pumalink  $\chi^2$  calculation of Eq 18. We have not yet found a way to exploit the very tiny volume that these extrapolations occupy in 6D space, and instead use an enclosing volume described by the parameters `dxmax` and `dwmax` for the allowable difference in unit vector and tangential velocity. These default parameters are not adjusted by PUMALINK for the time interval  $\Delta t$ , which is the main reason for the degradation in PD with increasing  $\Delta t$ .

For example, by doubling `dxmax` and `dwmax` for the ATLAS full night experiment, the median PD changed from 98.7% to 99.8%, and the parabolic decline of PD with lag time improved from 99.7%–94.5% for lags of 2–8 days to 99.9%–99.3%. This widened acceptance also caused the execution time to become 5 times longer and increased false alarms.

The choice of kd-tree search parameters is the primary tradeoff between performance closer than 0.1 AU and processing time, and the PUMALINK code is not as efficient as it could be in this regime. With the default parameters PUMALINK spends  $\sim 50$  microsec per kd-tree search to find each close pair of tracklets that is then passed to the pumalink algorithm, but only  $\sim 0.25$  microsec for the pumalink calculation to accept or reject them. More efficient sorting and pairing would allow the kd-tree parameters to be relaxed without a performance penalty.

- Once a pair of tracklets is known to be close in 6D space at the reference time, the pumalink  $\chi^2$  comparison tells us whether there really is a  $\rho, \dot{\rho}$  for which the two tracklets are statistically close to one another. The parameter `chimax` governs whether the pair will be rejected or kept as a possible quad. `chimax` may be increased to avoid losing very nearby objects whose puma extrapolation may not be well matched by a linear function of  $s, w$ , but at the cost of more false alarms.
- Quads that have been passed by the pumalink calculation then have their detections fitted by PUMA, and they are kept if  $\chi_v^2$  is less than `chinmax`. Again the false alarm rate rises rapidly with statistically unlikely values for `chinmax`, even though exceptional real objects may require it.
- The detection grouping carried out by PUMALINK is straightforward, but the grouping of quads by interpolation to the reference time is governed by the parameter `grptol`. It is possible to widen this, at the cost of putting multiple objects in the same group, or to tighten it, at the cost of failing to groups multiple quads of the same group.

### 3.7.2. *Balancing detection probability against false alarm rate*

After PUMALINK completes, there will typically be many false alarms. It is then the user’s responsibility to decide how to set the acceptance criteria: reducing false linkages almost certainly will also remove linkages of real objects.

It may be possible to adjust one or more parameters as in the ROC curves of Fig 6 to optimize PD and FAR, but the optimum is depends on the application. In some cases a detection might be so valuable that a huge FAR is acceptable and it’s worth spending additional resources to sort out the false alarms. In other cases even a small FAR not be acceptable because of harm to reputation. In the minor planet community, concern over wasted followup observations

spent chasing false alarms causes surveys to be very conservative about reporting possible objects to the MPC (which unfortunately also hinders the possibility of advancing two uncertain linkages to a certain one).

The detections that are provided to PUMALINK typically sample both real and false populations. The real population has a distribution of object brightness that typically grows as some sort of power law, as a result of distance and from intrinsic luminosity distributions. The false population results from statistical fluctuations, both Gaussian noise and non-Gaussian effects in difference images. Therefore the number of false versus real detections is very different as a function of the “SNR limit” cutoff, with the ratio of false to real detections growing rapidly for fainter cutoffs. This cutoff choice is outside of the purview of PUMALINK; nevertheless PUMALINK will form many false linkages from false detections. As long as the execution time is not too burdensome this can be advantageous, however, because a quad can now be evaluated on the basis of the probability that all four detections are real, not just each one separately.

To get a sense of the numbers, a given ATLAS night has  $\sim 10^{11}$  potential detections, corresponding to every positive-going excursion on a difference image. This is reduced by a factor of  $\sim 10^5$  to  $\sim 10^6$  by the detection process, which tries to identify every positive-going excursion that is consistent with the PSF shape, subject to an SNR cutoff that balances retention of real objects versus admitting excessive false alarms. In fact the ATLAS software detects and keeps all PSF-like excursions to the 3-sigma level, but only passes ones that exceed  $\sim 5$ -sigma. For Gaussian statistics about one in three million events exceed 5-sigma, so this reduction of the number of events by only  $10^5$  illustrates the heavy tails of the actual distribution of events in the ATLAS images.

All ATLAS detections are accompanied by measurements of the SNR of the detection, the extent of the detection if it is trailed, and the  $\chi^2_\nu$  agreement between the detection and the local PSF shape. Additional information available for each detection includes the image mask (including the location of cross-talk artifacts and saturated pixels), the image before differencing, the “wallpaper” image from previous observations, and the list of all known stars and asteroids. All of this information is given to a classifier that assigns probabilities that the detection may be real or false, and if false what it might be.

The ATLAS classifier does a decent job of distinguishing transients and variable stars from image artifacts, but it is not perfect and using it to cull the input detections given to PUMALINK has a cost. Our experiment with PUMALINK on the ATLAS nights used a classifier threshold of only 10% that the detection is real, and in so doing lost 12% of real, linkable asteroids that PUMALINK might have captured. This tradeoff exists so that MOPS can complete on a short timescale. The full night ATLAS experiment also removed all detection information indicating that an object trailed during the exposure (consistent with the `omega` cutoff). These cuts remove only a small fraction of all detections and do not significantly aid PUMALINK, and therefore should be carefully reconsidered when optimizing PUMALINK for the ATLAS application.

Given these detections, PUMALINK forms tracklets within `dtmax` and `omega` at each epoch, producing  $\sim 10^7$  for each epochs. This is a straightforward proximity search that makes no attempt to decide when a pair is plausible. For example the fact that detections might have a similar brightness or slight extendedness in the same direction is ignored.

There are altogether  $\sim 10^{14}$  pairs of tracklets which could form a quad, and the algorithm described here manages to distill this down to  $\sim 10^5$  output quads, depending on sorting and efficient algorithms to kept the execution time short. As we have seen, within this set of quads the probability of keeping real objects is extremely high, nearly 100%, particularly for few day time lags or widened acceptance criteria. However, among these quads there are typically only  $\sim 10^4$  real objects and so  $\sim 90\%$  of quads and groups in the PUMALINK output are linkages of false detections or mis-linkages of real objects. There are a few quads which can be rejected with high certainty because PUMALINK finds them to be consistent with stationary objects ( $\chi^2_{\nu s} < 10$ ), but for the most part reducing the false alarm rate involves moving down the ROC curve and some real objects will be lost.

The simplest method to reduce the false alarms is to reject linkages with large PUMA  $\chi^2_\nu$ , i.e. move along the ROC curve of Fig 6. For the ATLAS nights we have seen that the knee in the ROC curve occurs at false alarm rates of around 50% and the loss of several percentage points in detection probability. We can do substantially better, however, by

1. formulating a better probability for each detection using all the information available,
2. making decisions based on PUMALINK’s groups,
3. re-examining the images themselves and re-classifying detections, and
4. seeking more detections that join onto PUMALINK’s linkages.

We will use the ATLAS full night experiment to illustrate each of these methods.

For ATLAS we have a number of pieces of information about each detection that were not fully exploited in the culling of input detections. First and foremost are the SNR of the detection and the  $\chi^2_\nu$  result when the detection was tested against the local PSF in the image. Additional information comes from the proximity to the edge of the detector where the noise enhancement from flatfielding is not perfectly modeled as well as the classifier output for faint detections. From the distribution of these detection characteristics for all the kast (which we know to be real) and non-kast (which are mostly false) we can form an ad-hoc probability function for detections (which is specific for ATLAS).

Figure 7 shows the distribution of the calculated SNR of all the ATLAS detections, and the distribution of this ad-hoc probability function for individual detections as well as the product for the detections that make up possible quads.

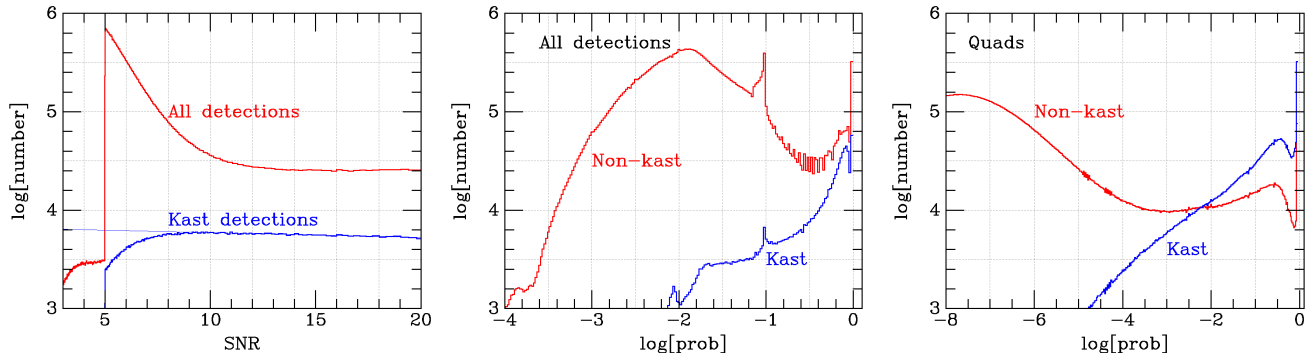


**Figure 7.** This figure shows the distribution of signal to noise for all detections (left), the distribution of the ad hoc probability function for all detections (center), and the aggregate probability function distribution for quads formed from the product of the probabilities of the 4 detections (right). In the left panel the SNR distribution cuts off abruptly at 5 because of the threshold applied to input detections. The count of kast detections rolls off below  $\text{SNR} \sim 8$ , and is down by about a factor of 2 at  $\text{SNR} \sim 5$  relative to the indicated extrapolation. In the middle panel the little spike at  $-1$  on the curves is caused by part of the ad-hoc probability function that puts a floor of 0.1 on the probability for detections with very large  $\chi^2_\nu$  for the PSF fit (in order not to eliminate comets, for example). In the right panel, the probability product is such a powerful discriminator that there are more kast quads at large probability than non-kast, unlike the distributions for each detection in the middle panel.

We calculate the probabilities for each detection, multiply them together for each output quad from PUMALINK to create an aggregate  $\log(P)$ , and then use different trial thresholds on that to select “good” quads. For these “good” quads we calculate ROC curves by varying the PUMA  $\chi^2_\nu$  cutoff, and make a new family of ROC curves shown in Fig 8. As we saw in Fig 7 the false alarms are greatly suppressed by requiring the detection probability product  $\log(P)$  exceed some threshold, and additional cuts from the PUMA  $\chi^2_\nu$  can reduce the FAR well below 5%. However, this comes at a cost — the detection probability is noticeably reduced as well. The best choice for  $\log(P)$  depends on the application, and the exact form and quality of  $\log(P)$  also depends on the information that the application has available.

The second method to improve the FAR exploits the grouping provided by PUMALINK. If the input to PUMALINK comprises more four observations of a field, PUMALINK will try to group quads that share detections and are consistent with one another. There are three possibilities for a given quad: 1) detections are not shared with any other quad, 2) detections are all shared by one of the groups that PUMALINK forms from proximate quads and the quad is absorbed into the group, and 3) some detections are shared with another quad, but other detections between these two quads are inconsistent with a single object.

In Case 1) the quad has to be considered on its own, as above. In Case 2) the quad has been absorbed into a group which has a much higher probability of being real than a single quad — in fact with application of the ad-hoc probability test just described almost all the groups of at least 5 detections that survive in the ATLAS experiment are mis-linkages instead of bogus detections.

Case 3) normally indicates a mis-linkage. A tracklet from one night might link to more than one tracklet from the other epoch. If detections from the tracklets are inconsistent with being from the same object because they are too far apart PUMALINK will refuse to merge these two quads or groups. The user then needs to identify these quads or groups

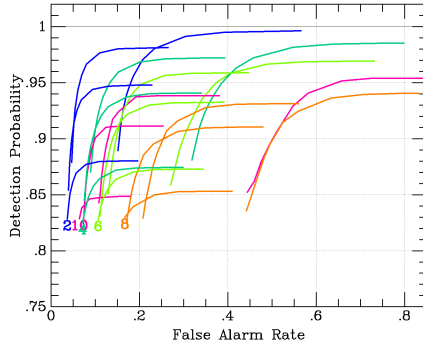


**Figure 8.** This figure shows PUMA  $\chi^2$  ROC curves for all the quads from the full night ATLAS experiments. As in Fig 6 the colors show the inter-epoch lag time: blue through magenta are lags from 2 to 10 days. The rightmost set of curves in each color show the results without post-PUMALINK probability cuts but with a cut on  $\chi^2_s$  to reject stationary objects and a cut to reject space velocity greater than 50 km/s. Moving to the left and lower false alarm rate are curves restricted to quads with  $\log(P) > -5$ ,  $\log(P) > -4$ , and  $\log(P) > -3$ .

that do share detections but are not linked together and endeavor to decide which is correct. Although both quads or groups may have an acceptable aggregate probability and PUMA  $\chi^2$ , it may be possible to decide on one or the other by which is more probable. Another method is to start assigning detections to objects using unambiguous quads or groups and by process of elimination rule out cross-linkages because they contain a detection already assigned to a different object.

As an example, there is a group of 5 detections in the PUMALINK between two of the ATLAS nights which looks like it is a very good candidate to be real, visually and by  $\log(P)$ . However, this group of 5 shares a detection called 01a58995o0404o.12134 with an even higher probability group of 7 but cannot merge with that group because it also shares a detection called 01a58999o0520o.6397 with a different group of 6. The group of 7 and the group of 6 are more likely to be real than the group of 5 by virtue of their size and having a higher probability. (As it turns out the group of 7 and the group of 6 are indeed two different kasts.) If those two detections are removed from the pool by virtue of being claimed by the group of 7 and group of 6, the group of 5 can be eliminated as a mis-linkage. A new, stand alone program that solves this Sudoku-like puzzle of PUMALINK mis-linkages could be very powerful.

The third method for reducing false alarm is reclassifying. Detections of real objects are usually distinguishable by eye from detections of noise, even if they both have good  $\log(P)$ . The ATLAS classifier does not use a trained, machine learning test on all detections but ATLAS does use such a test once MOPS links detections as potential moving objects. The performance is excellent: 99.6% TP for only 9% FP (Chyba Rabeendran & Denneau 2021). The reason to delay the application of a machine learning classifier until PUMALINK has been run is twofold: execution time is faster because only a subset of detections are linked and need to be classified, and as above with  $\log(P)$  the aggregate classification of a group of detections can be much more incisive than on each on individually.

Finally, validation of a potential linkage by finding other detections that also belong essentially eliminates false alarms. This can be done on lower likelihood detections, such as the ATLAS 3-sigma file by using PUMA to interpolate all groups to the time and observatory location of exposures and counting the number of nearby detections. In the case that there are more than two exposures per epoch the detections may already exist in the input list, and helping PUMALINK’s simple grouping function can provide a useful count.

Similarly, the experiments above only compare PUMALINK performance on 2 nights at a time. Bringing in extra nights so that PUMALINK is hierarchically combining 3 or 4 epochs of tracklets reduces the false alarms and mis-linkages essentially to zero. All of these methods require knowledge that survey exposures exist at a given time and sky location, so that the count of nearby detections can be balanced by the count of exposures where the object was not seen. The MPC isolated tracklet file, for example, does not lend itself to statistical rejection of a possible tracklet, only confirmation.

All of these methods to suppress false alarms are application specific and therefore cannot be part of the core PUMALINK processing. Even in the case that many linkages are uncertain, perhaps because of few detections over a large time span, the PUMALINK output does offer a very compact way of digesting all the detections into potential linkages in a way that is easily saved and processed if and when new data become available, or tested against old

data or data from other observatories. PUMALINK can accept detections from any time and any observatory, the only requirement is that two detections must exist per object at two different epochs. (The PUMA library itself doesn't care at all about pairs or tracklets, of course.)

#### 4. CONCLUSION

With four (soon five) sites the ATLAS project to find dangerous asteroids is facing new challenges and opportunities for scheduling and linking detections of asteroids. In order to succeed in this linking it is mandatory to have at least 4 detections, at least for faint detections that do not have distinguishing characteristics such as being trailed. This requirement does not mean that the observations have to come from the same observatory, nor that the observations have to be closely contemporaneous. The ATLAS system can perform better when the different sites cooperate with one another to cover the sky every night, so the system needs to be able to efficiently link detections over time spans of one day or more, driven by the various site's longitude and weather.

This paper describes the software that ATLAS uses to fit orbits to sets of detections (PUMA), and a new methodology to find correct linkages between a set of undifferentiated observations (PUMALINK).

The PUMA algorithm for fitting orbits to angular positions on the sky is several orders of magnitude faster than the methods currently in use by the community such as `openorb` and `find_orb`, but it does not sacrifice accuracy. By taking advantage of the precision of the angular positions and by avoiding the usual predictor-corrector extrapolation strategy of differential equation integrators, PUMA can determine a 3D fit to 2D points on the sky in a millisecond. This opens the door for swift hypothesis testing on different sets of detections that might or might not be of the same object.

PUMA uses carefully chosen polynomials to extrapolate beyond the time interval of constraining observations, so the accuracy depends on the ratio between the extrapolation interval  $\Delta t$  and the time span  $\delta t$  of input observations. For  $\Delta t/\delta t < 1000$  PUMA typically manages errors of 10's of milliarcsec, with quadratic degradation as  $\Delta t/\delta t \gg 1000$ . Similarly, the ratio of the extrapolation interval and the "collision time"  $\rho/\dot{\rho}$  (the distance divided by the radial velocity) governs the non-linearity of the trajectory. PUMA explicitly uses the gravity of Sun, Earth, and Moon individually so it retains its accuracy when  $\dot{\rho}/\rho \Delta t \gtrsim 1$ .

The new PUMALINK algorithm operates on pairs of pairs of detections (pairs of tracklets), deciding which are consistent with a real orbit. PUMALINK has similarities to other approaches, notably HeliLinC, but it functions well at asteroid ranges of a small fraction of an AU. PUMALINK's effectiveness arises from the use of the Earth-Moon barycenter as the origin for PUMA, and it computes all possible trajectories of a tracklet as a linear function of the unknown distance and radial velocity. The probability that some distance and radial velocity can make two tracklets consistent at a given reference time is then a simple, explicit formula from these linear function coefficients. It is therefore possible to test 10 million possible tracklets against one another in a half hour of computer time. The accuracy of the PUMA library ensures that the linkages are accurate, even at distances much closer than the Moon, and the false alarm rate is manageable, even for linkages of only 4 detections over multiple days.

We demonstrated the performance of PUMALINK on three datasets that each span two weeks. The first was a set of full ATLAS nights, with two sites each observing a quarter sky in a declination band, following one another every other day. In addition to asteroids, these data have a very large number of stationary variables and transients as well as bogus detections. The second dataset was an opposition field (with many known asteroids) that various ATLAS sites observed at least 4 times every night with a quadrupled exposure time. The third dataset was an LSST simulation of all the moving objects that LSST might see over 2 weeks.

For all three experiments we formed all pairs of nights, gave them to PUMALINK for linking, and then evaluated the performance. We found that PUMALINK achieved a very high probability of detection (well above 95%) at a modest false alarm rate (less than 50%). The detection probability is better when PUMALINK is given a pair of nights that have a small extrapolation ratio ( $\Delta t/\delta t \lesssim 300$ ) but even for large extrapolation ratios ( $\Delta t/\delta t \gtrsim 3000$ ) the detection probability is still above 95%. This false alarm rate refers to a minimal set of 4 detections to form a quad between two nights. Linkage groups with more than 4 detections have a much smaller false alarm rate, and if PUMALINK were given more than two nights of observation the false alarm rate would be essentially zero.

Any linkage algorithm must balance detection probability, execution time, and false alarm rate. The optimal balance between these three factors is application specific and therefore does not have a unique solution to which PUMALINK can aspire. We discussed four methods to augment the PUMALINK output to trade these three against each other. For example, we reduced the false alarm rate in the full night ATLAS experiment by an order of magnitude at the same

detection probability by exploiting an ATLAS detection specific probability that all four detections making a linkage are real.

For ATLAS our goal is to implement PUMALINK, quadruple our normal exposure times, and observe fields only 3 times every other night instead of 4 times each night. This should improve our detection probability for nearby, approaching asteroids while also increasing the discovery rate of ordinary NEOs. The performance of such a revised schedule and linking will be reported in a future paper.

## 5. ACKNOWLEDGEMENTS

Support for the ATLAS system was provided by NASA grants NN12AR55G, 80NSSC18K0284, 80NSSC18K1575, and this work was supported by NASA grant 80NSSC23K0376. We are grateful for the LSST data set provided by Ari Heinze, the MPC ITF supplied by Matt Holman, and many discussions with Larry Denneau. This paper was substantially improved following recommendations of an anonymous referee.



## REFERENCES

- Alard, C. & Lupton, R. H. 1998, *ApJ*, 503, 325.  
doi:10.1086/305984
- Becker, A., 2015, *Astrophysics Source Code Library*,  
<http://adsabs.harvard.edu/abs/2015ascl.soft04004B>
- Bellm, E. C., Kulkarni, S. R., Graham, M. J., et al. 2019,  
*PASP*, 131, 018002. doi:10.1088/1538-3873/aaecbe
- Bernstein, G. & Khushalani, B. 2000, *AJ*, 120, 3323.  
doi:10.1086/316868
- Chambers K. C., Magnier, E. A., Metcalfe, N., et al., 2016,  
arXiv, arXiv:1612.05560
- Denneau, L., Jedicke, R., et al. 2013, *PASP*, 125, 357
- Drake, A. J., Djorgovski, S. G., Mahabal, A., et al. 2009,  
*ApJ*, 696, 870. doi:10.1088/0004-637X/696/1/870
- Graham, M. J., Kulkarni, S. R., Bellm, E. C., et al. 2019,  
*PASP*, 131, 078001. doi:10.1088/1538-3873/ab006c
- Granvik, M., Virtanen, J., Oszkiewicz, D., et al. 2009,  
*M&PS*, 44, 1853. doi:10.1111/j.1945-5100.2009.tb01994.x
- Heinze, A. N., Tonry, J. L., Denneau, L., et al. 2018, *AJ*,  
156, 241. doi:10.3847/1538-3881/aae47f
- Heinze, A., Eggl, S., Juric, M., et al. 2022, *AAS/DPS*  
Meeting Abstracts
- Holman, M. J., Payne, M. J., Blankley, P., et al. 2018, *AJ*,  
156, 135. doi:10.3847/1538-3881/aad69a
- Ivezić, Ž., Kahn, S. M., Tyson, J. A., et al. 2019, *ApJ*, 873,  
111. doi:10.3847/1538-4357/ab042c
- Juric, M., Kantor, J., Lim, K.-T., et al. 2017, *Astronomical*  
*Data Analysis Software and Systems XXV*, 512, 279.  
doi:10.48550/arXiv.1512.07914
- Juric, M., Eggl, S., Jones, L., et al. 2021, *AAS/DPS*  
Meeting Abstracts
- Kochanek, C. S., Shappee, B. J., Stanek, K. Z., et al. 2017,  
*PASP*, 129, 104502. doi:10.1088/1538-3873/aa80d9
- Licandro, J., Tonry, J., Alarcon, M. R., et al. 2023,  
arXiv:2302.07954. doi:10.48550/arXiv.2302.07954
- Moeyens, J., Jurić, M., Ford, J., et al. 2021, *AJ*, 162, 143.  
doi:10.3847/1538-3881/ac042b
- NRC 2010, *Defending Planet Earth: Near-Earth-Object*  
*Surveys and Hazard Mitigation Strategies: Final Report.*  
2010. Washington, DC: The National Academies Press
- Ofek, E. O., Ben-Ami, S., Polishook, D., et al. 2023,  
arXiv:2304.04796. doi:10.48550/arXiv.2304.04796
- Chyba Rabeendran, A. & Denneau, L. 2021, *PASP*, 133,  
034501. doi:10.1088/1538-3873/abc900
- Tonry, J. L., Denneau, L., Heinze, A. N., et al. 2018, *PASP*,  
130, 064505
- Tonry, J. L., Denneau, L., Flewelling, H., et al. 2018, *ApJ*,  
867, 105. doi:10.3847/1538-4357/aae386
- Zackay, B., Ofek, E. O., & Gal-Yam, A. 2016, *ApJ*, 830, 27.  
doi:10.3847/0004-637X/830/1/27